Locations and Mechanisms of Ocean Ventilation in the High-Latitude North Atlantic in an Eddy-Permitting Ocean Model

GRAEME A. MACGILCHRIST,[a,g] HELEN L. JOHNSON,[a] DAVID P. MARSHALL,[b] CAMILLE LIQUE,[c] MATTHEW THOMAS,[d,e] LAURA C. JACKSON,[f] AND RICHARD A. WOOD[f]

[a] *Department of Earth Sciences, University of Oxford, Oxford, United Kingdom;* [b] *Department of Atmospheric, Oceanic and Planetary Physics, University of Oxford, Oxford, United Kingdom;* [c] *Université Brest, CNRS, IRD, Ifremer, Laboratoire d'Océanographie Physique et Spatiale, IUEM, Brest, France;* [d] *National Oceanic and Atmospheric Administration/Geophysical Fluid Dynamics Laboratory, Princeton, New Jersey;* [e] *University Corporation for Atmospheric Research, Boulder, Colorado;* [f] *Hadley Centre, Met Office, Exeter, United Kingdom*

(Manuscript received 21 April 2020, in final form 27 August 2020)

ABSTRACT: A substantial fraction of the deep ocean is ventilated in the high-latitude North Atlantic. Consequently, the region plays a crucial role in transient climate change through the uptake of carbon dioxide and heat. However, owing to the Lagrangian nature of the process, many aspects of deep Atlantic Ocean ventilation and its representation in climate simulations remain obscure. We investigate the nature of ventilation in the high-latitude North Atlantic in an eddy-permitting numerical ocean circulation model using a comprehensive set of Lagrangian trajectory experiments. Backward-in-time trajectories from a model-defined North Atlantic Deep Water (NADW) reveal the locations of subduction from the surface mixed layer at high spatial resolution. The major fraction of NADW ventilation results from subduction in the Labrador Sea, predominantly within the boundary current (~60% of ventilated NADW volume) and a smaller fraction arising from open ocean deep convection (~25%). Subsurface transformations—due in part to the model's parameterization of bottom-intensified mixing—facilitate NADW ventilation, such that water subducted in the boundary current ventilates all of NADW, not just the lighter density classes. There is a notable absence of ventilation arising from subduction in the Greenland–Iceland–Norwegian Seas, due to the re-entrainment of those waters as they move southward. Taken together, our results emphasize an important distinction between ventilation and dense water formation in terms of the location where each takes place, and their concurrent sensitivities. These features of NADW ventilation are explored to understand how the representation of high-latitude processes impacts properties of the deep ocean in a state-of-the-science numerical simulation.

KEYWORDS: North Atlantic Ocean; Atmosphere-ocean interaction; Lagrangian circulation/transport; Ocean circulation; Boundary currents; Diapycnal mixing

1. Introduction

Ocean ventilation describes the process by which mixed layer properties, including temperature, salinity, and dissolved gases such as oxygen, carbon dioxide, and chlorofluorocarbons, are transported into and around the ocean subsurface. In the high-latitude North Atlantic Ocean, relatively dense isopycnals outcrop at the surface, facilitating ventilation of the deep ocean (Dickson and Brown 1994; Lazier et al. 2001). Properties translated to the ocean interior in this region are transported southward in the lower limb of the Atlantic meridional overturning circulation (AMOC; Lozier 2012), returning to the surface predominantly in the Southern Ocean (Talley 2013) after a residence time in the deep ocean on the order of centuries (Gebbie and Huybers 2010; Khatiwala et al. 2012). Consequently, through the long time-scale sequestration of anthropogenic carbon (Sabine et al. 2004; Khatiwala et al. 2009), and the uptake and distribution of heat (Abraham et al. 2013; Zanna et al. 2019), ventilation of the high-latitude North Atlantic plays a crucial role in transient climate change and regional variations of sea level rise. (Church et al. 1991; Boé et al. 2009; Katavouta et al. 2019).

Ventilation of the ocean interior on interannual and longer time scales requires that properties be both transported out of the surface mixed layer and remain in the subsurface (i.e., avoid being returned to the mixed layer), making ventilation an intrinsically Lagrangian process (Stommel 1979; Williams et al. 1995). Consequently, traditional observations have struggled to shed light on many critical aspects of deep North Atlantic Ocean ventilation (Lozier 2010; Bower et al. 2019). Eulerian observations of mixed layer evolution (Yashayaev 2007; Yashayaev and Loder 2016; Våge et al. 2011) and dense water formation (Marsh 2000; Isachsen et al. 2007) reveal characteristics of local subduction, but fail to resolve the subsequent pathways or retention of ventilated water. On the other hand, tracer observations (Talley and McCartney 1982; Kieke et al. 2006; Rhein et al. 2007) and Lagrangian floats (Lavender et al. 2000; Palter et al. 2008; Bower et al. 2009) in the subsurface ocean reveal the broad pathways and transit

Denotes content that is immediately available upon publication as open access.

[g] Current affiliation: Atmospheric and Oceanic Science, Princeton University, Princeton, New Jersey.

Corresponding author: G. A. MacGilchrist, graemem@princeton.edu

DOI: 10.1175/JCLI-D-20-0191.1

time scales of ventilated waters, but the turbulent (and consequently diffusive) nature of ocean circulation obscures detailed information on their origin (MacGilchrist et al. 2017). Consequently, many aspects of deep North Atlantic Ocean ventilation—including the locations and mechanisms of subduction from the mixed layer, the role played by the subpolar gyre boundary current, and the nature of subsurface pathways—remain obscure (Lozier 2010; Bower et al. 2019).

In this paper, we investigate the representation of deep North Atlantic Ocean ventilation in a global hindcast simulation of an eddy-permitting numerical ocean circulation model. We do so by directly linking subsurface waters to their location and time of subduction via backward-in-time Lagrangian trajectories. The approach is complementary to tracer-based, Green's function approaches (e.g., Deleersnijder et al. 2001; Haine and Hall 2002; Primeau 2005) that derive probability distributions for the times and locations of subduction, with the advantage that Lagrangian trajectories allow us to derive this information at higher spatial and temporal resolution for a fraction of the computational cost. In addition, whereas the Green's function approach requires the assumption of a steady flow pattern, our analysis allows us to evaluate time scales and pathways associated with a time-varying velocity field.

Our analysis is focused on the specific manner in which ventilation—including both subduction from the surface mixed layer and transport in the subsurface—is achieved in a state-of-the-science ocean-sea ice model; one that is typical of the ocean-sea ice components of models in the Coupled Model Intercomparison Project (CMIP). Such models show wide variations in their representation of processes critical to Atlantic Ocean ventilation and its variability, such as mixed layer depths in the subpolar gyre (Boé et al. 2009; Kuhlbrodt and Gregory 2012; Heuzé 2017) and the strength, depth and variability of the AMOC (Heuzé 2017; Beadling et al. 2018). Consequently, variable representation of the ventilation process is a major source of intermodel spread in the projection of ocean heat uptake (Boé et al. 2009; Kuhlbrodt and Gregory 2012) and carbon uptake (Frölicher et al. 2015).

In consideration of high-latitude ocean circulation, ventilation is often conflated with, and considered interchangeable with, dense water formation and overturning circulation (Naveira Garabato et al. 2017). Consequently, it is often presumed that they are dependent on the same dynamics, occur in the same locations, and/or vary on the same time scales. Ventilation, however, relates specifically to the dynamics of tracers and their connection to the surface ocean, such that the relevant processes can be markedly distinct and independent of dense water formation and overturning (Naveira Garabato et al. 2017; MacGilchrist et al. 2019). Recently, direct observations assessed the relative importance of different regions for the high-latitude AMOC (Lozier et al. 2019). Although the observations span only a short time window, they revealed that dense water formation in the Greenland–Iceland–Norwegian (GIN) Seas and northeastern subpolar gyre exerts the dominant influence on the strength and temporal variability of the overturning circulation, consistent with inference from prior observations and theoretical arguments (Spall and Pickart 2001; Spall 2004; Pickart and Spall 2007). In the course of this study, we consider the implications of this finding for the ventilation of the deep Atlantic Ocean. We show in particular that in the case of ocean ventilation the relative roles of the different regions are partially reversed, with the Labrador Sea now making the dominant contribution. Far from contradicting the recent observations, our results serve to emphasize this important distinction between dense water formation and ventilation.

2. Methods

a. Model details

The primary simulation used in this paper is a global implementation of the Nucleus for European Modeling of the Ocean (NEMO) model (Madec 2014). The simulation was carried out as part of the Drakkar project (Barnier et al. 2006). The ORCA025 configuration is used, which has a grid resolution of 1/4° (~27.75 km at the equator, refined at high latitudes) and 75 uneven vertical levels. The model is within the so-called "eddy-permitting" regime of ocean models. This means that, in most regions of the ocean, mesoscale features with length scales on the order of 50–100 km will be captured by 2 or 3 grid points (Hallberg 2013). As such, nonlinear behavior in the circulation emerges, but the full extent of ocean turbulence does not develop (Barnier et al. 2006). The grid is "tripolar," meaning that it converges at two points over land in the Northern Hemisphere, thus avoiding convergence in the Arctic Ocean. The ocean model is coupled to a thermodynamic sea ice model, LIM2 (Bouillon et al. 2009).

The simulation runs from 1958 to 2015 and is forced with historical atmospheric reanalysis. The reanalysis used is the "Drakkar Forcing Set 5," which is an updated version of the fields described in Brodeau et al. (2010). This forcing set is an adjusted version of the ERA40 reanalysis (Dee et al. 2011), with modifications applied to ensure approximate global near-balance of heat and freshwater, such that it can be used to drive interannual numerical ocean simulations. The simulation is initialized from rest with temperature and salinity from the Levitus climatological hydrography (Levitus et al. 1998), augmented with the Polar Science Center Hydrographic Climatology for the Arctic regions. With no spinup, the model fields undergo significant adjustment in the first 10–15 years, and results from these years should be treated with caution. Velocity, variable parameter (e.g., vertical diffusivity), and hydrographic fields are output as 5-day means.

To place the model solution in context, we compare the hydrographic structure and flow field in the subpolar North Atlantic to direct observations and derived observation-based products (Fig. 1). Further comparison of the model configuration with observations can be found in Grégorio et al. (2015) and Barrier et al. (2015). Figure 1, panels a through d, compares neutral density (calculated according to the empirical formulation of McDougall and Jackett 2005) along the section defined by the Overturning in the Subpolar North Atlantic Program (OSNAP) project, which spans across the Labrador Sea and the eastern subpolar gyre between Greenland and Scotland (Lozier et al. 2017; locations shown in Fig. 1e). Comparison is made with both direct observations of the 2015 annual mean and a long

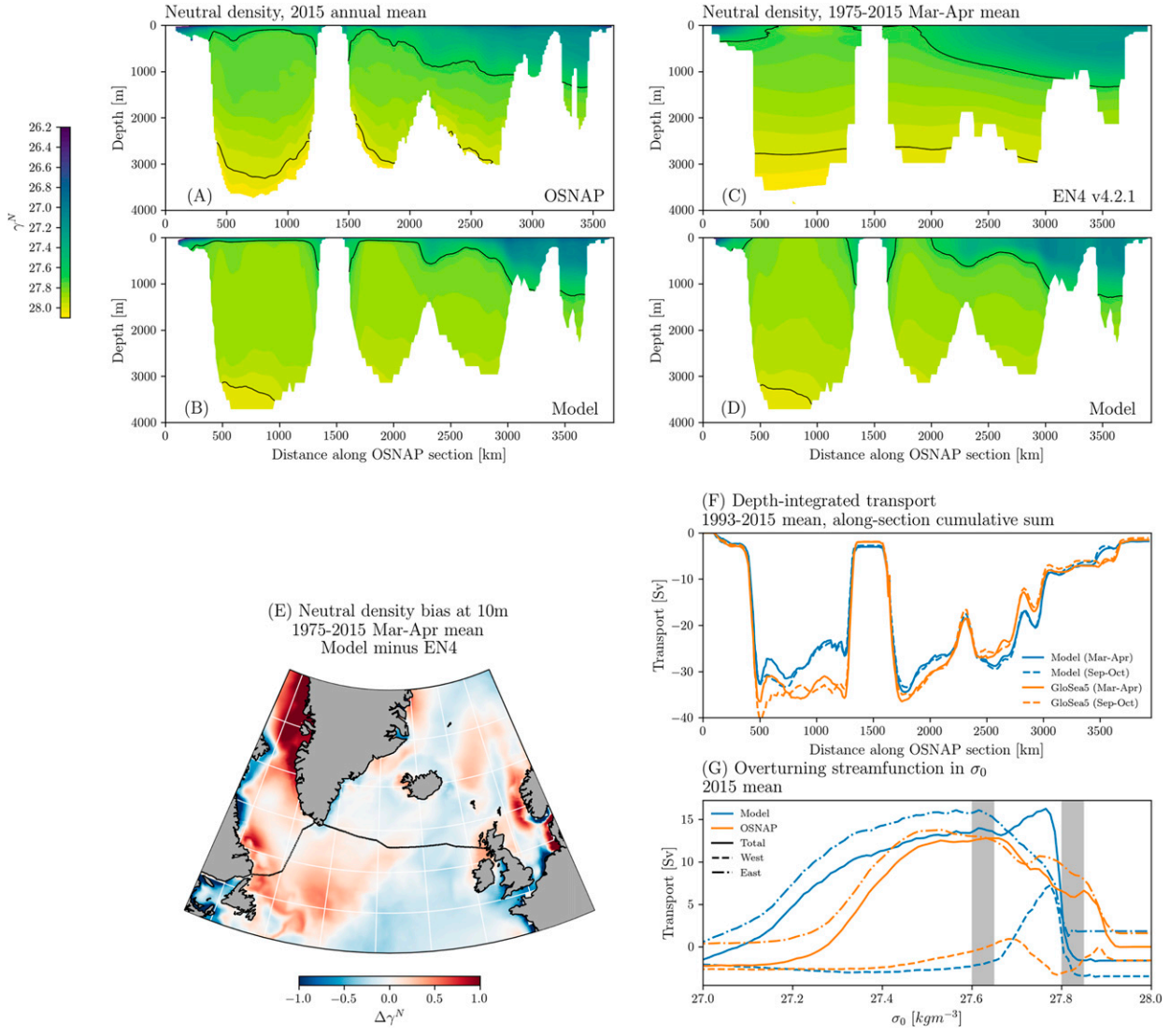

FIG. 1. Model–observation comparison in the North Atlantic subpolar gyre. (a) The 2015 annual mean neutral density from the OSNAP project (Lozier et al. 2017); (b) equivalent for the model simulation. (c) The 1975–2015, March–April mean neutral density from the EN4 v4.2.1 gridded observational dataset (Good et al. 2013), linearly interpolated onto the OSNAP line; (d) equivalent for the model simulation. (e) The location of the OSNAP section. Black lines show the upper and lower bounds of our model-defined North Atlantic Deep Water at $\gamma^n = 27.7$ and 28 kg m^{-3} (see section 2d). (e) Difference in 1975–2015, March–April mean neutral density at 10 m between the model simulation and EN4 datatset (linearly interpolated to model grid). (f) Cumulative, along-section sum of the depth-integrated volume transport along the OSNAP line for the model simulation (blue) and the GloSea ocean reanalysis product (MacLachlan et al. 2015; Zou et al. 2020; orange). Shown are the 1993 (due to limited time duration of GloSea) to 2015 means in both late-winter (March–April; solid lines) and late summer (September–October; dashed lines). (g) The 2015 annual mean overturning streamfunction in surface-referenced potential density coordinates for the model (blue) and OSNAP observations (orange). Shown are the overturning across the full OSNAP section (solid lines) as well as independently for the sections to the west (dashed) and east (dot–dashed) of Greenland. The gray patches show the approximate range of surface-referenced potential densities that correspond to the upper and lower bounds of our model-defined North Atlantic Deep Water. For all panels, data were extracted along the OSNAP line according to the approach of (Zou et al. 2020).

time-scale (1975–2015) late-winter (March and April) mean from the gridded observational product, EN4 (Good et al. 2013). While the observed stratification is broadly reproduced, the comparison reveals two relevant biases: comparatively low middepth (1000–2000 m) stratification, particularly in the Labrador Sea; and an absence of the densest observed water masses. Concomitant with the model's low middepth stratification is the annual late-winter occurrence of deep convection in the Labrador Sea, which substantially exceeds depths measured in observations (Barnier et al. 2006; Rattan et al. 2010). Comparison of late-winter surface densities from the EN4 dataset (Fig. 1e) shows that the model is marginally too dense in the western subpolar gyre

(consistent with overly deep mixed layers) and too light in the east. More substantial biases are present in coastal regions and in Baffin Bay (a proportion of this could be due to the low horizontal resolution of the derived observational product). Throughout our subsequent analysis, we discuss the results in the context of these known model biases.

In addition to the stratification, we also consider the fidelity of the model's velocity field and overturning circulation (Figs. 1f,g). In Fig. 1f we show the long-term mean, late-winter and late-summer, volume transport in the model and in a data-assimilating ocean reanalysis product, GloSea (MacLachlan et al. 2015; Zou et al. 2020). Notably, the boundary current in the Labrador Sea, and on the east side of Greenland, is between 5 and 10 Sv (1 Sv $\equiv 10^6\,m^3\,s^{-1}$) weaker in the model than in the ocean reanalysis. In Fig. 1g, we show the 2015 mean overturning circulation in potential density coordinates for the full OSNAP section (solid lines), and for the western (Labrador Sea; dashed lines) and eastern (northeast subpolar gyre; dot–dash lines) parts of the section. Here, the observations are taken directly from the OSNAP data. The magnitude of the overturning, as well as its division between the western and eastern sections is broadly well-represented by the model. Within the approximate density range of our model-defined "North Atlantic Deep Water" (see section 2d), demarcated by the gray patches, elevated transports in the model arise from a greater-than-observed overturning circulation in the Labrador Sea. Consistent with the absence of the densest waters (Figs. 1a–d), the model exhibits no overturning in that density range. The long-term (1993–2015) time-mean overturning circulation showed a pattern consistent with that presented here in both the model and the ocean reanalysis, GloSea.

b. Lagrangian trajectory evaluation

To evaluate trajectories in the numerical simulation, we use the Lagrangian analysis tool, Ariane (Blanke and Raynaud 1997). Ariane makes use of the fact that, for a steady velocity field and under the assumption that velocities vary linearly between gridcell faces, an analytical expression for the streamlines between gridcell faces can be defined. As a result, particles do not have to be explicitly evolved forwards in time (i.e., with a time-stepping scheme), but rather their future position can be evaluated directly from the streamline calculation. This makes the calculation of large numbers of trajectories extremely efficient.

To evaluate trajectories through a time-varying velocity field, we must assume that the field is piece-wise stationary. That is, that the velocity field changes in a discrete fashion at each time step. For the simulation used in this study, this means a discrete change in the velocity field at 5-day intervals. Trajectories can be evaluated both forwards and backward in time. Tracers, such as temperature, salinity and density, along trajectories are evaluated via trilinear (linear in the x, y, and z directions) interpolation from the closest surrounding model grid points at which the variable is defined. No attempt is made to parameterize subgrid-scale physics through the addition of stochastic noise as is done in other Lagrangian codes (van Sebille et al. 2018).

c. Experimental approach

We wish to determine the Lagrangian properties, namely the time and location of subduction, of the points in the deep North Atlantic throughout our numerical ocean simulation. To this end, we evaluate backward-in-time trajectories from a volume within the deep North Atlantic (see section 2d), and determine the last time and location that that water was in the mixed layer. The volume of deep North Atlantic water can then be partitioned based on, for example, the location where it left the mixed layer (subduction location), its density at the time of subduction, or the water-column depth in the region of subduction.

Particles were initialized at each model tracer point (located in the center of the grid cell) at the end of September every year between 1976 and 2015 (we avoid the early, spinup years of the simulation). Although the simulation is global, we bound the particle trajectories between approximately 30°S and 80°N. As such, no information is derived from advective pathways originating in the mixed layers north and south of these boundaries. These pathways make up a negligibly small contribution (on the order of 1%) to the ventilation of our model-defined NADW. Ventilation of the ocean interior, below the seasonal pycnocline, happens over a limited time period each year; an effect known as Stommel's demon (Stommel 1979; Marshall et al. 1993). As a result, in considering ventilation on interannual and longer time scales, it is sufficient to evaluate the Lagrangian properties at only one point in time each year, since the signature of seasonal ventilation is eroded annually (Williams et al. 1995). Trajectories were evaluated backward in time until reaching a density that was within 0.01 $kg\,m^{-3}$ of the density at 10 m, following Thomas et al. (2015). Our primary results are insensitive to this definition of mixed layer depth.

The use of purely advective trajectories enables us to link points in the subsurface to unique properties associated with their subduction from the mixed layer. However, the absence of a stochastic parameterization for subgrid-scale motion (e.g., Shah et al. 2011; Koszalka et al. 2013; Shah et al. 2017) is a source of uncertainty in the pathways of these trajectories. Likewise, through the use of 5-day mean velocity fields, our trajectory calculation omits sub 5-day variability in the model velocity field. Encouragingly, recent work suggests that the resolved scales in eddy-permitting models (such as that used in this study) are sufficient to capture much of the diffusive spreading of tracers (Rühs et al. 2013; Gillard et al. 2016; Kamenkovich et al. 2017), including when evaluated using temporally averaged velocity fields (Gary et al. 2011). Furthermore, the spatial distribution of age derived from our purely advective trajectories (not shown) is broadly consistent with that derived from tracer observations in the ocean (Rhein et al. 2015). This suggests advection by the resolved velocity field captures the main components of the ventilation pathways. As such, we are confident that the absence of a diffusive parameterization in our trajectories does not qualitatively affect our main results or conclusions.

d. Identifying North Atlantic Deep Water

The bounding surfaces of the volume of water we consider were chosen to capture all of the deep ocean ventilation in the

North Atlantic, which we hereafter collectively label North Atlantic Deep Water (NADW).[1] It does not make sense to choose these boundaries based on observations of ventilated surfaces in the North Atlantic ocean, since model hydrography can deviate substantially from the real ocean (Fig. 1). Instead, we choose to consider the volume bounded between neutral densities $\gamma^n = 27.7$ and $28\,\mathrm{kg\,m^{-3}}$, and present the justification for this below. For comparison with historical classifications of NADW (which use potential density referenced to 2000 m), the mean σ_2 of our upper bound is $36.9 \pm 0.03\,\mathrm{kg\,m^{-3}}$ and of our lower bound is $36.62 \pm 0.03\,\mathrm{kg\,m^{-3}}$ (where the $\pm$ value represents one standard deviation). In the ocean, the upper and lower bounds of North Atlantic–sourced deep water are traditionally taken as $\sigma_2 = 36.5$ and $36.99\,\mathrm{kg\,m^{-3}}$ (Yashayaev 2007; van Sebille et al. 2011), suggesting that the ventilated portion of the model's deep Atlantic basin has a comparatively narrow density distribution, consistent with Fig. 1.

The time-mean surface density distribution at high northern latitudes during late winter in the model simulation is shown in color in Fig. 2a. Outcropping density surfaces between $\gamma^n = 27$ and $28.5\,\mathrm{kg\,m^{-3}}$ are present in the region, with the densest isopycnals outcropping in the GIN Seas and along the west coast of Greenland. A local maximum in surface density is also apparent in the Labrador Sea. Notably lighter surface densities coincide with the Arctic outflows along the east coast of Greenland and from Baffin Bay along the south west of the Labrador Sea. Isopycnal outcrops corresponding to our definition of NADW are shown with black contours. The contours bound the Labrador Sea, with the lighter surfaces outcropping around the boundary and the outcrop for $\gamma^n = 27.9\,\mathrm{kg\,m^{-3}}$ appearing in the northwest region. The upper bound of the volume ($\gamma^n = 28\,\mathrm{kg\,m^{-3}}$) excludes the central GIN Seas, such that the dense water formed in that region is not included in our definition of NADW.

The volumetric distribution of neutral density in the whole of the Atlantic sector of the model (30°S–80°N, 100°W–30°E) is shown in Fig. 2b, where we only show densities greater than $\gamma^n = 27\,\mathrm{kg\,m^{-3}}$. Most of the volume is contained between $\gamma^n = 27.7$ and $28.2\,\mathrm{kg\,m^{-3}}$, with distinct peaks at around 27.85 and 28.05. Also shown is the neutral density distribution of the volume ventilated in an experiment in which particles were initialized throughout the entire sector in the final winter of the simulation. Over the 54 years of the simulation, ~10% of the Atlantic domain was ventilated from the mixed layer and, in the deep ocean, this was concentrated between $\gamma^n = 27.7$ and $28\,\mathrm{kg\,m^{-3}}$, with a single peak at $\gamma^n = 27.85\,\mathrm{kg\,m^{-3}}$. The remaining, unventilated volume centered around the peak at $\gamma^n = 28.05$ is Southern Hemisphere–sourced bottom water that has moved northward into the basin across the southern boundary of our trajectory experiments.

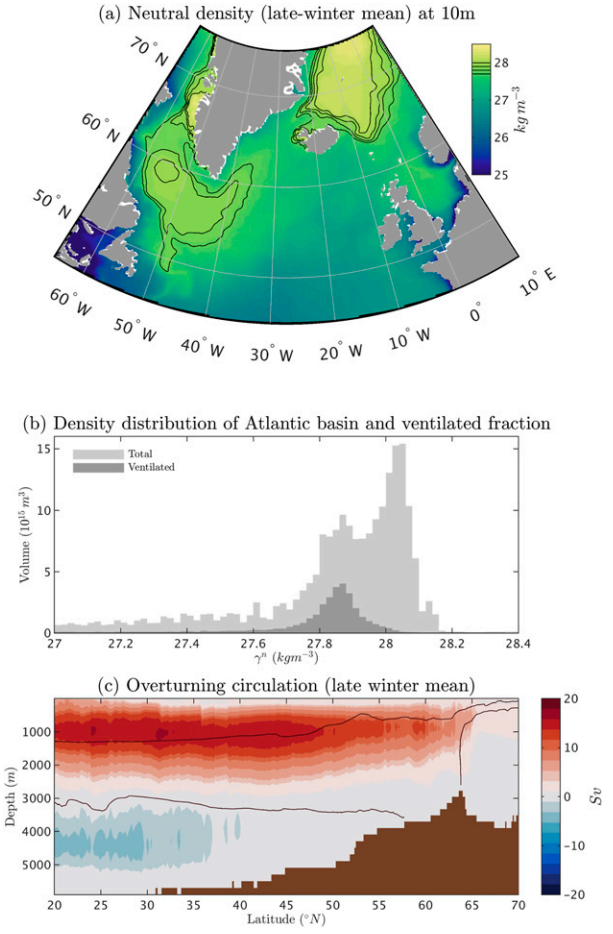

FIG. 2. (a) Late-winter mean (March–April mean from 1975 to 2015) neutral density γ^n distribution at a depth of 8 m. Solid lines correspond to densities between $\gamma^n = 27.7$ and $28\,\mathrm{kg\,m^{-3}}$ at $0.1\,\mathrm{kg\,m^{-3}}$ spacing. (b) Volumetric distribution of density across the entire Atlantic basin (between 30°S and 75°N) shown in light gray bars, and the same for the ventilated fraction, shown in dark gray. (c) Late-winter mean Atlantic meridional overturning circulation: zonally integrated northward volume transport ($1\,\mathrm{Sv} = 10^6\,\mathrm{m^3\,s^{-1}}$) cumulatively integrated from the bottom to the surface. Overlain dark contours correspond to late-winter mean neutral density contours at $\gamma^n = 27.7$ and $28\,\mathrm{kg\,m^{-3}}$.

There is ventilation in density classes greater than $\gamma^n = 28\,\mathrm{kg\,m^{-3}}$ (Fig. 2b) that we omit in our main experiments. To ensure that this does not result in us missing an important component of deep North Atlantic ventilation, we looked more closely at this water mass through forwards-in-time Lagrangian experiments (see section 3c). These experiments revealed that only a very small fraction (less than 5%) of all of the water denser than $\gamma^n = 28\,\mathrm{kg\,m^{-3}}$ (ventilated and unventilated) is exported south of 60°N and into the main North Atlantic basin. Ventilated water with $\gamma^n > 28\,\mathrm{kg\,m^{-3}}$, therefore, is almost entirely GIN Seas water that remains mostly within the GIN Seas and as such does not make a significant contribution to the NADW that this study focuses on.

[1] We adopt the term "North Atlantic Deep Water" to describe all of the water ventilated in the high-latitude North Atlantic. Elsewhere in the literature this term is used to identify water formed primarily in the GIN Seas as distinct from the "Labrador Seawater" formed in the subpolar gyre.

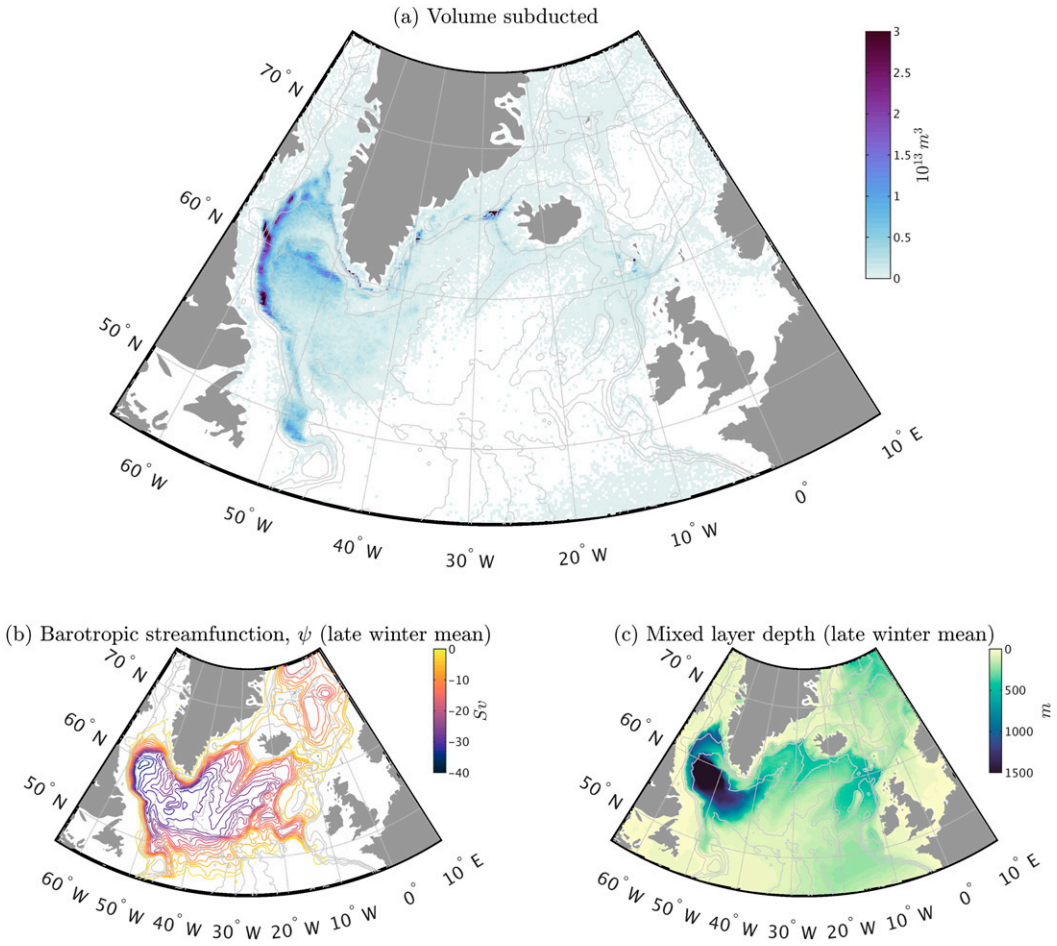

FIG. 3. (a) Locations where ventilated NADW was subducted from the mixed layer. (b) Late-winter mean (March–April mean from 1975 to 2015) barotropic streamfunction ψ. (c) Late-winter mean mixed layer depth (evaluated during the simulation using a density difference criterion of $\Delta\rho = 0.01\,\mathrm{kg\,m^{-3}}$, consistent with that used in our Lagrangian trajectory experiments). In all panels, light gray lines correspond to bathymetric contours at depths of approximately 500, 150, 3000, and 3900 m.

Another aspect that we wish to capture in our selection of the volume boundaries is the southward flow of NADW as the lower limb of the AMOC. Figure 2c shows the AMOC streamfunction at the end of June in the final model year. This is overlain with contours of neutral density, averaged across the North Atlantic basin (excluding the Mediterranean), at $\gamma = 27.7$ and $28\,\mathrm{kg\,m^{-3}}$. This shows clearly that the volume bounded between $\gamma^n = 27.7$ and $28\,\mathrm{kg\,m^{-3}}$ captures the major component of the southward limb of the AMOC. The upper boundary at $\gamma^n = 27.7$ sits marginally below the northward flowing limb at subtropical latitudes and thus it makes sense not to consider lighter water masses. The lower boundary sits marginally below the boundary between the upper and lower overturning cells (where the sign of the streamfunction changes sign). As explained above, only a small fraction of water denser than $\gamma^n = 28\,\mathrm{kg\,m^{-3}}$ is ventilated in the North Atlantic meaning that the main constituent of this southward transport is transformed Antarctic Bottom Water.

3. Results

a. *Ventilation by subduction in the Labrador Sea boundary current*

Establishing the locations at which ventilated NADW subducted from the mixed layer is a crucial step toward determining the key mechanisms driving ventilation. In the high-latitude North Atlantic, wintertime heat loss to the atmosphere drives convective deepening of the mixed layer (Lazier et al. 2002). These deep mixed layers of course imply local ventilation, but whether each of these subducted water masses goes on to ventilate the wider Atlantic basin or whether they are re-entrained into the mixed layer downstream is not clear.

The volume of ventilated NADW that subducted from the mixed layer at each grid cell (over the full course of the simulation) is shown in Fig. 3a. The broad pattern follows that of the wintertime mixed layer depth (Fig. 3c)—an indicator of the dominant regions of convective dense water formation (Lazier et al. 2001)—in that the spatial range coincides with that of

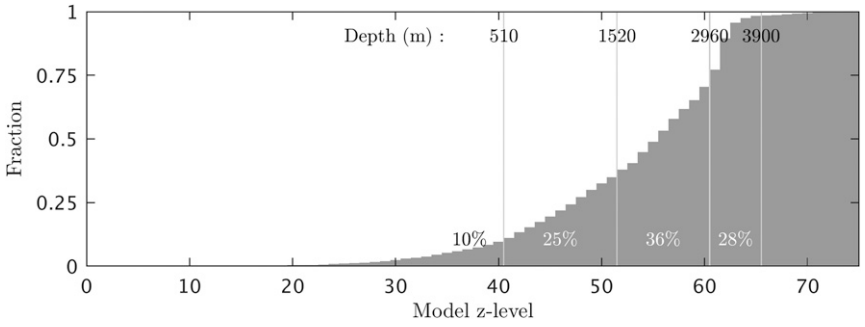

FIG. 4. Cumulative volumetric distribution of the water column depth in the grid cells where subduction occurs (i.e., Fig. 3a) distributed as a function of bathymetric contour (model z level). Vertical gray lines delineate the bathymetric contours displayed in Fig. 3 at depths of approximately 500, 1500, 3000, and 3900 m. Percentages at the bottom of the panel correspond to the amount of ventilated NADW water subducted between these contours.

mixed layers exceeding approximately 500 m. However, in terms of the regions where subduction makes the dominant contribution to NADW ventilation, the patterns of wintertime mixed layer depth and subducted volume are notably distinct. In particular, the most conspicuous feature of Fig. 3a is the dominance of subduction near the Labrador Sea boundary—a region that coincides with the subpolar gyre western boundary current (the Labrador Current; Lazier and Wright 1993), as revealed by the wintertime barotropic streamfunction (Fig. 3b). Furthermore, while there is some contribution from subduction in the central Labrador Sea, particularly in the northern region, it does not emerge as the major region of ventilation despite persistently deep winter mixed layers.[2] There is almost no contribution from subduction in the GIN Seas (discussed in detail in section 3c) despite broad regions of deep winter mixed layers. This discrepancy between the patterns of subduction and mixed layer depth emphasizes that the pathways of water following subduction—which determine whether water remains in the subsurface or is re-entrained to the mixed layer downstream—are crucial to the ventilation process.

The dominance of subduction in the boundary region for the ventilation of NADW is further emphasized by considering the distribution of ventilation as a function of water column depth, shown as a cumulative histogram in Fig. 4a. The vertical gray lines correspond to the bathymetric contours displayed in Fig. 3, with the percentage of the volume ventilated between these contours also shown. The majority of ventilation of NADW (72%) results from subduction that takes place over bathymetry shallower than 3000 m, with most of this (40% of total) occurring between water column depths of 1500 and 3000 m, within the Labrador Current. Open ocean subduction, which we classify as that occurring over bathymetry deeper than ~3000 m, accounts for around 28% of the total ventilation, the majority of which occurs in the Labrador Sea (Fig. 3a).

We wish to determine the processes setting the pattern of subduction in the boundary current. Subduction of water from the surface mixed layer can be considered as the sum of three processes (Cushman-Roisin 1987): shallowing of the mixed layer depth (detrainment); vertical motion resulting from horizontal convergence in the mixed layer; and horizontal motion across a sloping mixed layer base (so-called lateral induction). Over an annual cycle, if the mixed layer deepens by the same amount each year, detrainment is small (Marshall et al. 1993). Vertical motion in the upper ocean (not shown) is noisy, with the largest values present in coastal regions, but does not show any consistency with the pattern of subduction. Consequently, we expect that the pattern of subduction identified in Fig. 3 may be set by the horizontal flux of water across a sloping mixed layer base. Indeed, this has previously been noted to be the case in the subtropical regions of the Atlantic and Pacific (Marshall et al. 1993; Marshall and Marshall 1995; Qiu and Huang 1995).

We investigate horizontal flow across the mixed layer base as a description of subduction in the boundary current by considering mixed layer depths along streamlines of the barotropic streamfunction. The late-winter mixed layer depth in the Labrador Sea sampled on streamlines of the late-winter barotropic streamfunction (Fig. 3b) is shown in Fig. 5a where the marker size corresponds to the volume of subduction at that point (taken from Fig. 3a) and the color corresponds to the winter-mean mixed layer depth (taken from Fig. 3c). Following the cyclonic flow of the boundary current, we note that elevated subduction on the western boundary closely corresponds with the region where there is a substantial horizontal gradient in the mixed layer depth. This is shown more clearly in panels Figs. 3b and 3c where we "unwrap" the streamlines to show late-winter mixed layer depth (Fig. 3b) and subducted volume (Fig. 3c) along streamlines as a function of distance around the Labrador Sea starting in the north east. Along the streamlines, the mixed layer deepens from around 200 m in the north east

[2] The model winter mixed layer depth in the central Labrador Sea is notably deeper than observed in the ocean (Holte et al. 2017). This is a well-known bias in the NEMO model (Barnier et al. 2006), the possible origin of which we discuss further in section 3c. Note that it is also probable that the bias itself is overestimated here due to the way that mixed layer is measured in the model output (Courtois et al. 2017).

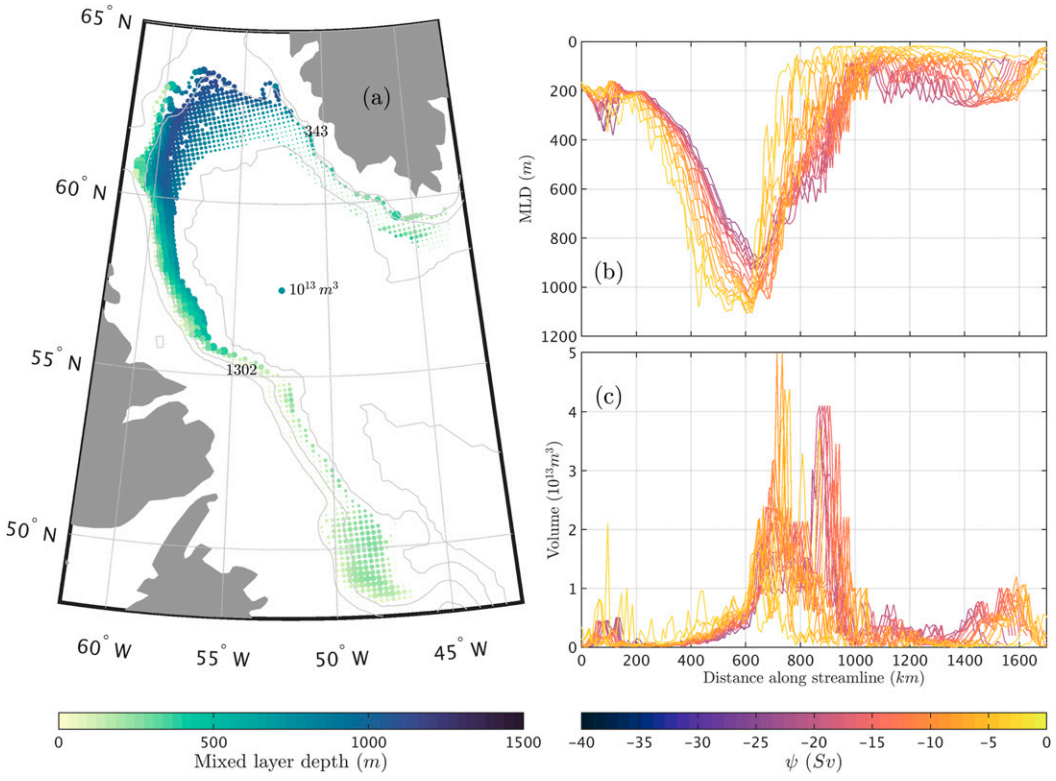

FIG. 5. (a) Late-winter mean mixed layer depth (colors; from Fig. 3c), sampled along late-winter mean barotropic streamlines (from Fig. 3b), where the size of each point represents the volume of ventilated NADW subducted at each location (from Fig. 3a). Light gray contours are the same as those in Fig. 3 at approximately 500, 1500, 3000, and 3900 m. A representative distance along the streamline is shown in two locations at approximately 340 and 1300 km for ease of reference in (b) and (c). (b) Mixed layer depth along the streamlines of (a). (c) Volume of ventilated NADW subducted along the streamlines of (a).

to a maximum of approximately 1000 m after a distance of between 400 and 700 km. Over this region, subduction is generally low. Mixed layer depths then decrease sharply to shallower than 200 m between 600 and 1000 km along the streamline. Regions of elevated subduction correspond closely to this decrease in the mixed layer depth, even to the extent that maxima in subducted volume (at around 700 km for $\psi \approx -8$ Sv and 900 km for $\psi \approx -20$ Sv) correspond to the sharpest gradients in mixed layer depth along these streamlines. This close correspondence continues around the south west of the Labrador Sea, with elevated subduction between 1400 and 1700 km aligning with a decrease in the mixed layer depth toward the Grand Banks (around 50°N, 48°W).

The formulation of Cushman-Roisin (1987) is purely kinematic and, on its own, offers limited insight on the dynamics of the subduction process itself. Here, it highlights that the dynamical processes of primary importance are those establishing the structure of the horizontal flow and shape of the winter mixed layer base. We can derive some qualitative understanding of these from Fig. 5, which highlights a crucial role for deep mixed layers in the north west of the Labrador Sea, near the entrance to Baffin Bay. Viewed from the Lagrangian perspective of a water column flowing around the boundary, the along-stream gradient in the late-winter mixed layer depth is likely set by convection in this north west corner followed by relatively rapid restratification (presumably by lateral freshwater fluxes from the coastal regions; Pennelly et al. 2019) as the water moves southward. This results in a bolus of newly ventilated water moving rapidly away from the regions of deepest mixed layers, allowing ventilation of the wider North Atlantic basin. It is worth noting that while the stratification and strength of the Labrador Sea boundary current are broadly well reproduced in the model (Fig. 1), the overall positive bias in the late-winter mixed layer density and discrepancies in the middepth stratification could impact subduction in the region. However, there is no obvious spatial structure to these biases that would suggest a role in establishing the patterns noted in Fig. 5.

It is notable that this process of lateral induction is also apparent in the open ocean region. In this region, the maximum in subduction occurs at the northern edge of the deep convection region, where the mixed layer depth shallows sharply toward the north. The curving contours of the barotropic streamfunction illustrate that in this region the time-mean flow recirculates within the Labrador Sea (a feature observed by Lavender et al. 2000), drawing water from the convective

region toward the boundary current. It thus appears that ventilation via water subducted in the open ocean is facilitated by the direction of the time mean flow in relation to the sloping mixed layer base (also noted by Palter et al. 2008).

To summarize, the majority of NADW ventilation results from subduction within the Labrador Sea boundary current, with a smaller contribution from subduction in the open ocean. Subduction in the boundary current is affected by the flux of water across a sloping winter mixed layer base, the pattern of which is set by deep convection at the northern edge of the Labrador Sea followed by restratification as water flows southward along the western boundary.

b. *Ventilation via subsurface transformation*

In the ocean, distinction between ventilation arising from subduction in the boundary current and that from open ocean convection is generally based on the density class into which subduction occurs (Pickart 1992). Freshwater input from glacial and sea ice melt results in stronger stratification in coastal regions relative to the open ocean such that the deepest density surfaces do not commonly outcrop near the boundary (Fig. 2a). However, intermediate densities with indistinguishable characteristics are formed in both the boundary regions (Pickart et al. 1997) and the open ocean (Kieke et al. 2006). Furthermore, the deepest density classes formed by deep convection have been observed to form directly in the boundary current, under extreme surface forcing conditions (Pickart et al. 2002; Cuny et al. 2005). We wish to establish, therefore, if and how subduction in the boundary current and open ocean are distinguished by density in our experiments.

In Fig. 6, we show density distributions of the volume subducted over distinct bathymetric ranges (i.e., water column depth). We present the distributions for both density at subduction (dashed lines) and density in the subsurface at the end of the simulation (solid lines). At subduction the density distribution (dashed lines) is broadly consistent with what we would expect from considering the locations of density surface outcrops (Fig. 2a): over shallow bathymetry, subduction occurs into lighter density classes; over deep bathymetry, subduction occurs into both intermediate and the most dense NADW classes. However, it is clear that a fraction of the subduction within the boundary current (even that occurring over bathymetry shallower than 1500 m) goes on to ventilate water in the densest density classes. Intermediate densities (around $\gamma^n = 27.85\,\mathrm{kg\,m^{-3}}$), which constitute the most abundant volume in NADW (Fig. 2b), are ventilated by subduction across all bathymetric ranges, predominantly those deeper than 1500 m. Following transportation in the subsurface, density distributions for subduction in different bathymetric ranges are much less distinct (solid lines). The volume subducted in the shallowest regions has become, on average, notably more dense, while the most dense volume subducted in the open ocean ($\gamma^n > 27.9\,\mathrm{kg\,m^{-3}}$) has become lighter. The result of these subsurface transformations is that ventilation across the whole NADW density range arises from subduction in both the boundary current region and the open ocean.

Over much of the ocean subsurface, away from ocean boundaries, parcels of water are exposed to relatively low

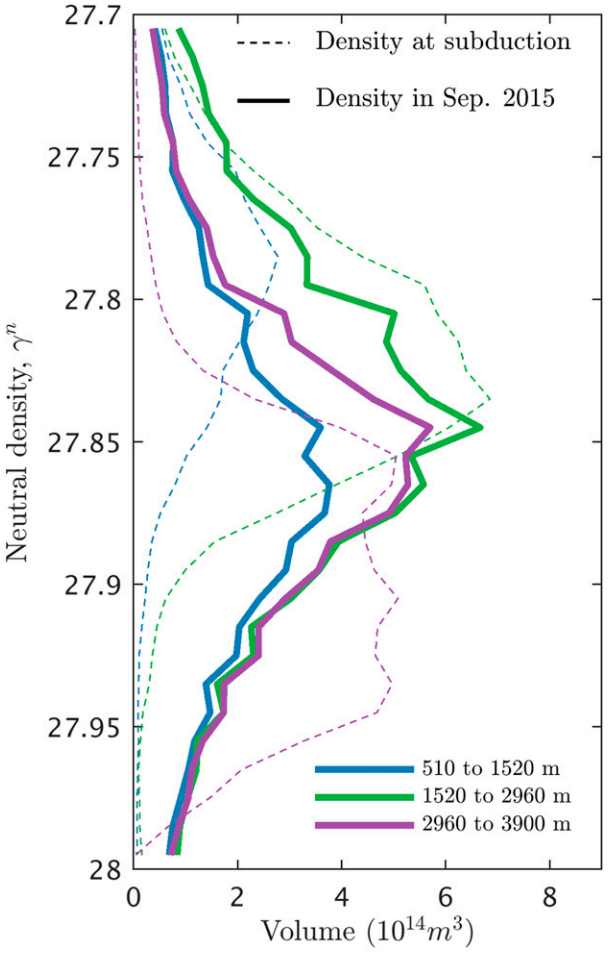

FIG. 6. Volumetric distributions of density separated by the water column depth of the location where subduction occurs (colors), for densities at the time of subduction (dashed lines) and densities at the end of the simulation (solid lines).

levels of diapycnal mixing (Ledwell et al. 1993; Waterhouse et al. 2014). In the absence of mixing, fluid parcels will flow in the direction that conserves their locally referenced potential density, that is, along neutral surfaces (McDougall 1987). Consequently, ventilation pathways in the subsurface are thought to be predominantly along rather than across neutral surfaces, and thus parcels of water are expected to approximately conserve their neutral density (caveats associated with the nonlinearity of the equation of state notwithstanding; McDougall 1987; Klocker and McDougall 2010). The fact that the ventilation of NADW has such a substantial contribution from subsurface transformation therefore merits further consideration.

We examine the density changes that occur in our experiments by plotting the volumetric joint distribution of density at subduction and in September 2015 (Fig. 7a). If trajectories perfectly followed neutral surfaces (as defined here based on the formulation of McDougall and Jackett 2005), the entire volume would fall along the one-to-one line (dashed black). Consistent with our expectation from Fig. 6, a substantial

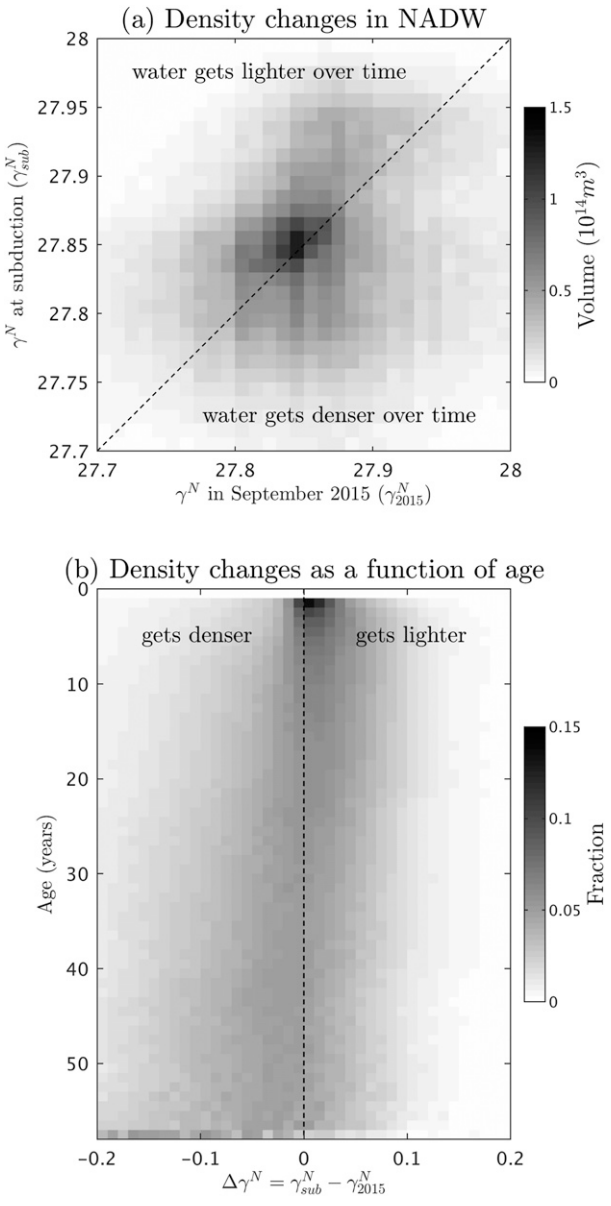

FIG. 7. (a) Volumetric joint distribution of the density of ventilated NADW at the time subduction and at the end of the simulation. Along the dashed line these densities are equal. (b) Volumetric density distribution of the density *difference* between subduction and September 2015 as a function of age. The distribution at each age is presented as a fraction of the total volume of ventilated NADW of that age.

amount of water resides away from this line, implying that it has moved across neutral surfaces in the ocean subsurface. A simple scaling argument suggests that a majority of these density changes are in excess of what would be expected for the canonical background level of diffusive mixing: $k_z = 10^{-5}\,\mathrm{m^2\,s^{-1}}$. It should be noted that most of the subsurface transformation occurs *within* NADW, but that a fraction of NADW ventilation does arise from transformation across the bounding density surfaces (~20%).

Water of all different ages contributes to Fig. 7a, and a better impression of how these density changes emerge is found by considering the distribution of density changes as a function of age (Fig. 7b). The first thing to note is that density changes are present even in water only a few years old. Particularly for the youngest waters, this could indicate a failing of the mixed layer definition, whereby the trajectories are exposed to diabatic forcing but not within the specified density range of the mixed layer. Progressing to older waters, the distribution becomes more diffuse and increasingly skewed to negative values indicating that a greater fraction of waters of that age have become more dense over time. This is indicative of a slow, diffusive process that is spreading particles across density surfaces while mixing the center of mass progressively downward through the stratification over time.

A first-step toward understanding the source of these density changes is to establish where they occur in the model domain. For this purpose, we evaluate the location and density of all of the ventilated particles (as of September 2015) every 5 days along their trajectories for the previous 10 years, or until they intersect the mixed layer. The mean rate of density change experienced by trajectories that cross each grid cell is shown in Fig. 8a (there is a logarithmic scale for both positive and negative rates of density change). Note that this picture emphasizes the regions in which the most substantial transformation takes place, but does not necessarily indicate that these transformations make the largest contribution to the broad transformations inferred from Figs. 6 and 7.

The most conspicuous feature in Fig. 8a is that the largest density changes occur close to bathymetry. This is predominantly close to the basin boundaries, but also includes a signature around the Mid-Atlantic Ridge wherever it shallows into the depth range of NADW. Some of the largest density changes are seen in the region of dense overflows—at the Greenland–Scotland ridge and the Mediterranean outflow—the former of which is considered in more detail in section 3c. Along much of the path of the deep western boundary current, the pattern of density changes (with water becoming lighter on the shoreward side and more dense on the oceanward side) is consistent with theoretical arguments for where dense waters will upwell and downwell through boundary layer mixing in an ocean basin with sloping sidewalls (Armi 1978; Garrett et al. 1993; Ferrari et al. 2016). However, such a pattern is clearly not consistent across the whole basin (e.g., in the Labrador Sea).

The imprint of bathymetry on the pattern of these density changes encourages us to consider how the model parameterizes mixing close to the bottom boundary. Figure 8b shows the wintertime-mean coefficient of vertical diffusion k_z one grid cell above the bathymetry. Enhanced values in coastal regions and along bathymetric features matches the distribution of the density changes seen along trajectories. In this configuration of NEMO, the vertical mixing coefficient is elevated close to bathymetry in an attempt to capture the impact of wave-generated mixing via flow over rough topography (MacKinnon et al. 2017). In addition, mixing coefficients can be further enhanced by frictionally generated shear in the bottom boundary layer that perturbs the weak local stratification,

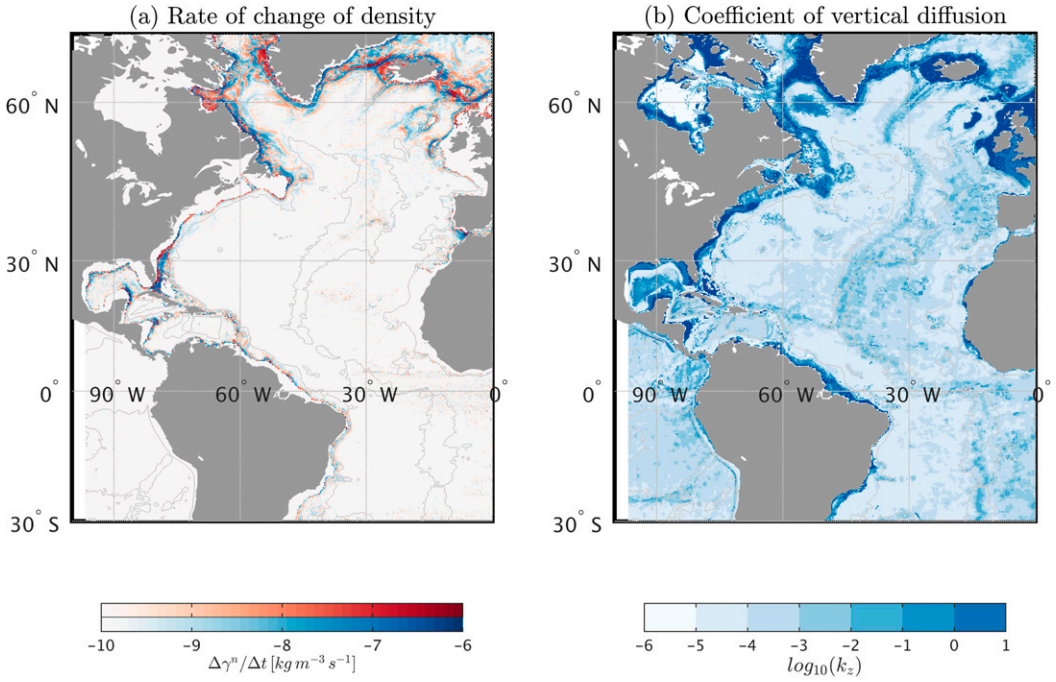

FIG. 8. (a) The rate of change of density ($\Delta\gamma^n/\Delta t$) along trajectories in the last 10 years of the simulation averaged at each grid cell. Only trajectories for ventilated NADW are included. The grid cell to which the density change is ascribed is the mean location of the particle between 5-day time steps. Negative density changes (particle moves to lighter water) follow the red color scale and positive density changes (particle moves to denser water) follow the blue color scale. Note that both color scales are logarithmic. The light gray contour corresponds to a depth of 3900 m. (b) Late-winter mean coefficient of vertical diffusion k_z one grid cell above the ocean bottom. The light gray contour corresponds to a depth of 3900 m.

which is parameterized in NEMO using a total kinetic energy closure scheme (Madec 2014). High values of k_z in the central Labrador Sea are a signature of the deep penetration of the surface mixed layer parameterization in this region. Note that mixing due to dense overflow waters (discussed in more detail below) is parameterized in the model predominantly as a horizontal rather than vertical process and thus would not have a signature in k_z. The vertical length scale of enhanced mixing close to bathymetry, set by the gridcell thickness, is on the order of hundreds of meters in the deep ocean and tens of meters near the coast.

To determine how this explicit model mixing impacts the density distribution of NADW, we trace k_z along trajectories. Figure 9c shows the distribution within each density class of the time-mean *order of magnitude* of k_z along trajectories. It is clear that along its subsurface pathway, NADW is exposed to levels of vertical mixing that are elevated on average relative to background levels ($1.2 \times 10^{-5}\,m^2\,s^{-1}$), particularly in the midrange and deeper density classes, where most of the ventilated NADW resides (Fig. 2b). This exposure to enhanced mixing is more than likely the result of interaction with parameterized vertical mixing near the bottom boundary. While qualitative in nature, these results provide reasonable evidence that explicit model mixing, namely parameterization of mixing close to bathymetry, can drive considerable subsurface transformation (and thereby ventilation) in NADW within the Atlantic sector. There are, of course, other potential contributors to the density changes seen in Fig. 7, including implicit model mixing (Griffies et al. 2000; Lee et al. 2002), the imperfect definition of neutral density (Klocker and McDougall 2010), and cumulative errors in the Lagrangian trajectory calculation (van Sebille et al. 2018). We note in particular that Megann (2018) evaluated implicit model mixing to be at least of similar magnitude as parameterized mixing in a related configuration of the NEMO ocean model, making it likely that this also contributes to the subsurface transformation seen along ventilation pathways. Evaluating the relative impact of these different processes is beyond the scope of the present study.

c. *An absence of ventilation from subduction in the GIN Seas*

In the ocean, the GIN Seas are a major source water for the deep Atlantic basin (LeBel et al. 2008). Dense water formed by convective activity in the region flows southward over shallow sills between Greenland and Scotland. Entrainment of ambient water as the dense water flows over these sills leads to the modification of water mass properties and an approximate doubling of the total volume transport (Girton and Sanford 2003; Mauritzen et al. 2005; Legg et al. 2009). The resultant water masses, known as overflow waters, form the densest categories of North Atlantic Deep Water. Inventories of

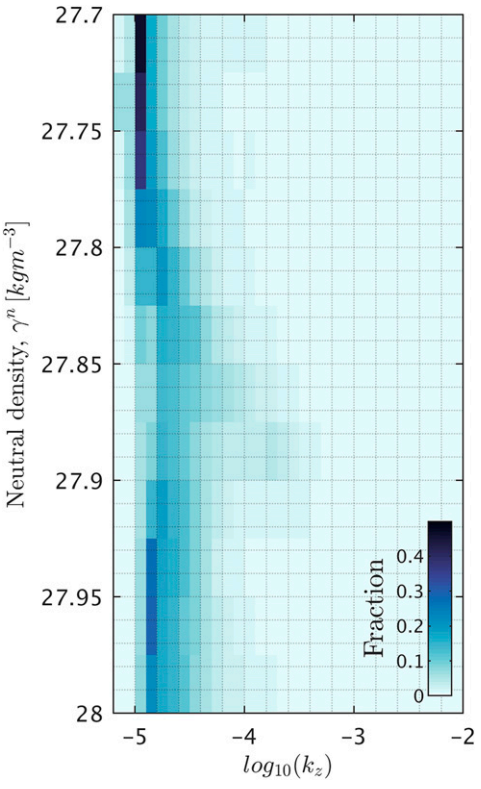

FIG. 9. The distribution of the mean order of magnitude of vertical diffusion coefficient k_z along each trajectory in each density class of ventilated NADW (where density class corresponds to the density at the end of the simulation). For each density class, the distribution is presented as a fraction by dividing by the total number of trajectories in that density class.

chlorofluorocarbons (CFCs) indicate that between 30% and 40% of recently ventilated water in the deep Atlantic basin is contained within these overflow waters (LeBel et al. 2008). Accounting for the doubling in volume by entrainment, this suggests that between 15% and 20% of ventilated water in the deep Atlantic basin arises from subduction in the GIN Seas.[3] In our simulation, however, only approximately 4% of all ventilated NADW in the Atlantic basin was subducted in the GIN Seas. Note that this number pertains to the experiment in which particles were initialized at every tracer point in the basin (section 2d), and thus also includes water with densities greater than 28 kg m^{-3}. Consistent with this result, comparison of the model stratification with observations (Fig. 1) revealed an absence of the very densest waters in the subpolar gyre, despite their presence in the surface of the GIN Seas (Fig. 2a).

We investigate the reason for the relative absence of ventilation arising from subduction in the GIN Seas using a forwards-in-time Lagrangian experiment. Particles are initialized below the mixed layer in the GIN Seas in September 1975, and followed forward in time until they are re-entrained to the mixed layer, or until the end of simulation if they remain in the ocean subsurface. Note that this experiment includes particles that were both ventilated and unventilated in 1975, so the following discussions does not only pertain to "ventilated" GIN Seas water. In Fig. 10a we show the latitude that these particles reached before the end of the simulation, presented as a *cumulative* distribution. The dark blue bars show the fraction of the decrease between each latitude band that is due to the re-entrainment of particles into the mixed layer (the remaining fraction is made up of particles that continue to circulate in the subsurface in each latitude band). That the fraction at 80°N is not 1 is due to the fact that a small number of particles (6%) were exported across the northern boundary. Moving south from the most northerly latitude, the rapid decrease from the initial volume implies that only around half of the initialized volume made it out of the GIN Seas (~65°N). Further attenuation over the latitudes of the Labrador Sea means that only around 12% of GIN Seas water makes it south of ~45°N (recalling that this includes both recently ventilated and unventilated GIN Seas water, the fraction contributing to NADW ventilation is smaller still). The main reason for this attenuation over the latitude band of the Labrador Sea is re-entrainment to the surface mixed layer, the locations of which are shown in Fig. 10b (water recirculating within the subpolar gyre is a much smaller contribution). Unlike the pattern of subduction (Fig. 3a), the locations of re-entrainment are spread across the Labrador Sea, occurring wherever the time-mean mixed layer is relatively deep (Fig. 3b).

Dense water formed in the GIN Seas is considerably more dense than that in the Labrador Sea, as evidenced by the outcropping isopycnals in Fig. 2a. As such, it could only be re-entrained in the Labrador Sea were its density to be substantially reduced along its southward pathway. As noted above, mixing between the dense overflows and ambient water at the Greenland–Scotland ridge means that lightening of GIN Seas water is to be expected as it flows into the main Atlantic basin. Indeed, in Fig. 8a we noted that some of the most substantial density changes take place in the vicinity of the Greenland–Scotland ridge, making it likely that water exiting the GIN Seas undergoes substantial subsurface transformation. Figure 10c shows the shift in density distribution between initialization and re-entrainment for the volume that is re-entrained to the mixed layer south of the GIN Seas. There is a 0.6 kg m^{-3} shift of the distribution peak toward lighter classes at the time of re-entrainment, and a narrowing in the density range between γ^n = 27.6 and 27.9 kg m^{-3}. This indicates that subsurface mixing of GIN Seas water is sufficient to erode the deep stratification and make it susceptible to re-entrainment as it transits the deep mixed layers of the Labrador Sea.

4. Discussion

Accurate representation of ocean ventilation will be crucial in determining the fidelity of the next generation of climate projections, particularly their ability to predict transient and regional climate change (Bahl et al. 2019; Katavouta et al. 2019). Here, we have used a Lagrangian

[3] This assumes that all of the modes of North Atlantic Deep Water take up CFCs at an equal rate, and that entrained ambient waters and GIN Seas water contribute equally to the downstream CFC inventory.

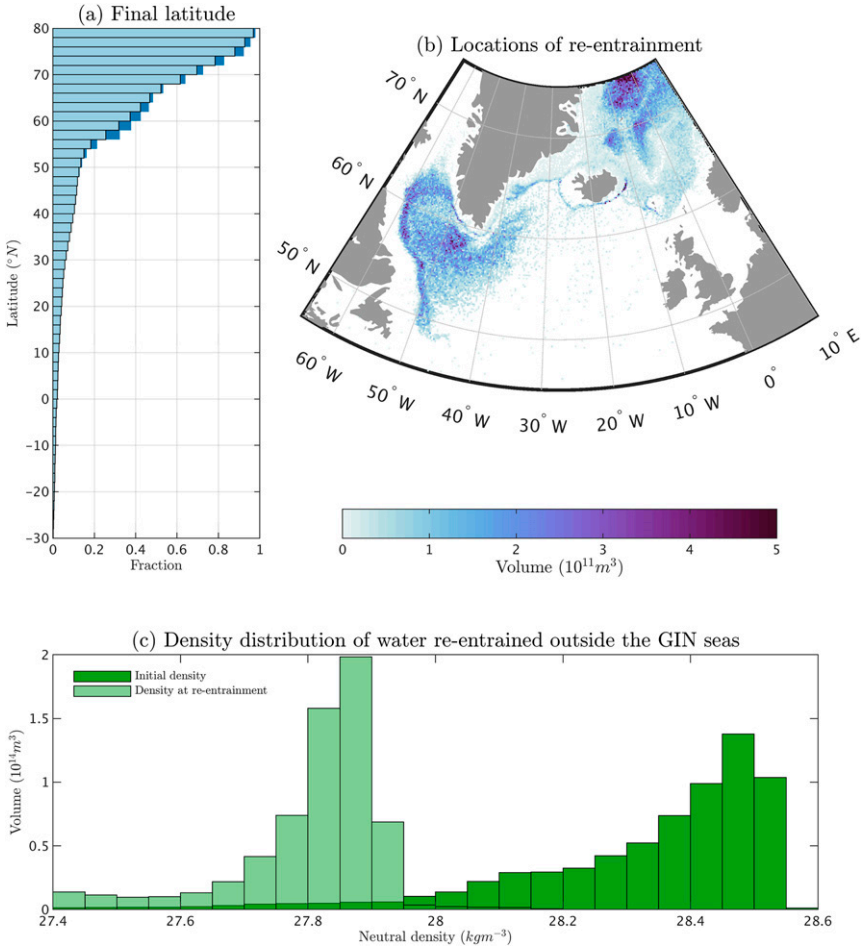

FIG. 10. (a) Cumulative volumetric distribution (summing from south to north and dividing by total volume) of the latitude reached by water initially in the GIN Seas from a forward-in-time Lagrangian experiment. The dark blue bars show the fraction of the step at each latitude that is due to re-entrainment of water into the mixed layer. (b) Volume of water re-entrained at each grid cell. (c) Volumetric distribution of density for water re-entrained south of the GIN Seas (south of 65°N) when it was initialized in the GIN Seas (dark green) and at the time of re-entrainment (light green).

trajectory approach to better understand the nature of high-latitude North Atlantic ventilation in a CMIP6-grade numerical ocean-sea ice circulation model. Our analysis revealed three important characteristics of the ventilation process: (i) the dominant role of subduction in the Labrador Sea, particularly within the boundary current; (ii) the role of subsurface transformation in spreading ventilated waters across density classes; and (iii) the absence of ventilation arising from subduction in the GIN Seas. In the following, we discuss these characteristics and the mechanisms by which they arise in the simulation, exploring the implications for our understanding of both ocean ventilation and the fidelity of its representation in the model.

a. Dominance of the Labrador Sea in NADW ventilation

At first glance, the dominant role played by the Labrador Sea in NADW ventilation appears contradictory to recent work that plays down the role of the region in the large-scale overturning circulation (Lozier et al. 2019). This recent work has instead highlighted that the GIN Seas and northeast subpolar gyre are the regions of primary importance in dense water formation and overturning. The circulation in the model simulation used here is consistent with this picture (Fig. 1f). Although proportionately more potential density-space overturning takes place in the model Labrador Sea compared to observations, it still accounts for considerably less than half of the dense water formation in the NADW density range. To reinforce this picture, we show the long-term mean neutral density-space overturning streamfunction as a function of latitude (Fig. 11; equivalent to Fig. 2c transformed to neutral density surfaces). In this frame, we note that there is some transformation, especially across lighter density classes, occurring in northward flowing waters across the latitudes of the Labrador Sea (approximately 50°–64°N). However, the

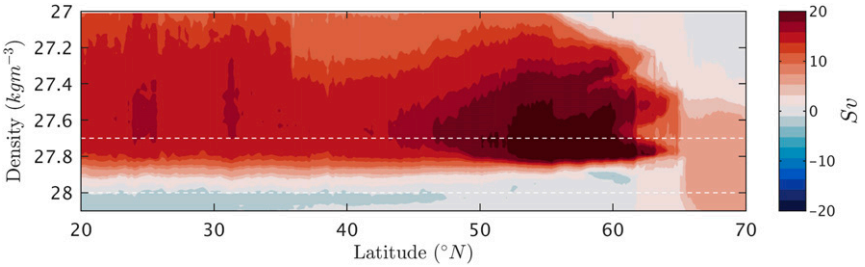

FIG. 11. Late-winter mean Atlantic meridional overturning circulation in density coordinates: zonally integrated northward volume transport ($1\,\mathrm{Sv} = 10^6\,\mathrm{m^3\,s^{-1}}$) cumulatively integrated from the densest to lightest surface. Overlain white dashed lines denote $\gamma^n = 27.7$ and $28\,\mathrm{kg\,m^{-3}}$.

majority of dense water formation occurs north of around 62°N, incorporating the northern rim of the Labrador Sea but poleward of the major subduction regions identified in our Lagrangian experiments (Fig. 3a). Consequently, southward flowing streamlines across the latitudes of the Labrador Sea are relatively flat.

This discrepancy between the regions of ventilation and of overturning serves to highlight the important distinction between these two phenomena (Naveira Garabato et al. 2017). Although water may transit the Labrador Sea without being substantially transformed in density, the occurrence of deep mixed layers (both in the boundary current and the open ocean) nevertheless exposes subsurface waters to the atmosphere prior to their southward export. Water arrives at the Labrador Sea rather dense, is made only marginally denser, but is still refreshed and ventilated via contact with the atmosphere. It is for this reason that in the tracer distribution of the deep Atlantic Ocean, there is such a dominant signature of the Labrador Sea (Talley and McCartney 1982; Rhein et al. 2015) despite the region's relative unimportance for the overturning circulation. In line with this, Zou et al. (2020) found that the impact of convective activity in the Labrador Sea over the time scale of the OSNAP observations (Lozier et al. 2019) was to change the subsurface ocean properties (temperature and salinity in this case) without invoking substantial density-space overturning.

While there is observational evidence for direct subduction in the boundary current (Palter et al. 2008), subduction in the open ocean by way of deep convection followed by exchange into the boundary current has been traditionally considered the dominant mechanism of NADW ventilation (Lozier 2010; Buckley and Marshall 2016). Contrary to this perspective, we noted in section 3a that ventilation of NADW in this simulation was predominantly effected by subduction directly within the Labrador Sea boundary current. More than 70% of ventilated NADW left the surface mixed layer over bathymetry shallower than 3000 m (Fig. 4). This was the case despite the persistent occurrence of deep mixed layers in the central Labrador Sea, making clear the importance of export pathways for the ventilation process. Using quasi-Lagrangian observations, Palter et al. (2008) argue that subduction directly within the boundary current is an important process in the formation of Labrador Seawater, and that it makes a comparable contribution to the boundary current heat budget as exchange with the open ocean. It is feasible, therefore, that the dominant role played by boundary current subduction in this model simulation reflects its underappreciated contribution to NADW ventilation in the ocean.

At the same time, the dominance of boundary current subduction raises questions about the model's representation of exchange between the boundary current and open-ocean. Transient eddy-driven exchange of tracers has been shown to make an important contribution to budgets in the Labrador Sea (Straneo 2006; Palter et al. 2008; Saenko et al. 2014; Howatt et al. 2018). Such exchange is likely to be suppressed in the model at this latitude due to the limited horizontal resolution (Saenko et al. 2014). Indeed, correspondence of the subduction pattern with time-mean properties of the horizontal circulation and mixed layer depth (Fig. 5; including for the central Labrador Sea), support the suggestion that time-varying (eddying) processes are of secondary importance. On the other hand, Gillard et al. (2016), who used a configuration of the same numerical model as that employed here, showed that increasing the horizontal resolution threefold (from 1/4° to 1/12°) resulted in only relatively minor changes in the advective exchange between the boundary current and open ocean. It is plausible, therefore, that the role of direct ventilation via the boundary current would persist in experiments run at higher resolution (i.e., when transient eddy activity is better resolved in the region). It is important to note that the absence of advective exchange (the aspect of tracer transport represented by Lagrangian trajectories in the absence of a stochastic mixing parameterization) does not preclude the possibility that parameterized diffusive exchange of tracers between the boundary current and open ocean could still be taking place and making a contribution to NADW ventilation.

The pattern of subduction for NADW ventilation is evidently sensitive to the representation of the boundary current stratification. In particular, subduction arises from the occurrence of deep mixed layers as the boundary current rounds the north west corner of the Labrador Sea (Fig. 5). Observations of mixed layer depth (Holte et al. 2017; de Boyer Montégut et al. 2004) do not reveal this feature in the ocean, suggesting that it could be indicative of model bias (although wintertime observations in this region are scarce, even in the Argo era). Figure 1e further reveals that the density of the late-winter

mixed layer in the boundary current is greater than in observations. The proximity to outflows from the Canadian Arctic Archipelago and Greenland means that the local stratification is sensitive to the transport of freshwater out of these regions (Straneo and Saucier 2008; Curry et al. 2011). The implication, therefore, is that representation of these freshwater transports could have a direct impact on the location where NADW leaves the mixed layer.

The location where ventilation of NADW takes place—whether it is primarily through subduction in the boundary current or open ocean—has implications for the future role of the North Atlantic in transient global warming. In particular, ongoing uptake and sequestration of anthropogenic carbon and heat will depend on how the stratification in these two regions changes. Arctic freshwater outflow and glacial melt are projected to increase in a warming world (Holland et al. 2006; Koenigk et al. 2007; Fettweis et al. 2013), but the extent to which the added freshwater will remain within the boundary current or be exported into the open ocean remains uncertain (Gillard et al. 2016; Luo et al. 2016). Previously, much attention has been focused on open ocean convection (due to its apparent link to the AMOC; Swingedouw et al. 2015). Our results indicate that trapping of freshwater in the boundary current could have a similarly notable climate impact through its effect on ventilation. Considering Lagrangian perspectives on NADW ventilation under climate change, as in Lique and Thomas (2018), could help to establish the relative importance of these different impacts.

b. *NADW ventilation through subsurface transformation*

In section 3b, we noted that a considerable fraction of the NADW in this simulation is ventilated via subsurface transformation (Fig. 6) due, in part, to parameterized vertical mixing. The role of internal mixing in subsurface tracer transport is of interest due to its impact on ocean heat and anthropogenic carbon uptake (Groeskamp et al. 2016), biogeochemical cycles (Tuerena et al. 2019), and the closure of the large-scale overturning circulation (Ferrari and Wunsch 2009; de Lavergne et al. 2016b). Improved understanding of the nature and distribution of internal mixing (Waterhouse et al. 2014; MacKinnon et al. 2017) has invited efforts to understand its impact on subsurface tracer distributions and ensure that they are well represented in global climate models (Mashayek et al. 2017; de Lavergne et al. 2016a; Holmes et al. 2019).

The subsurface transformation of ventilated NADW occurred, at least in part, through the parameterization of vertical mixing close to bathymetry whereby trajectories in the deep ocean interact with regions of elevated background vertical diffusion (Fig. 9). This is consistent with Mashayek et al. (2017) who note that substantial cross-isopycnal tracer transport can be achieved via intermittent interaction with mixing "hotspots"—regions of elevated mixing close to the ocean floor. Indeed, when considered over a broad scale, this can lead to tracer transports an order of magnitude greater than would be inferred from the mean level of diffusion at the mean depth of the tracer. Our results serve to show that, first, this effect is broadly captured in a global, eddy-permitting simulation with a rather crude parameterization of bottom-intensified mixing, and second that it has a considerable impact on the character of NADW ventilation.

c. *Impact of overflow mixing parameterization on NADW ventilation*

In our Lagrangian experiments, the relative unimportance of the GIN Seas for NADW ventilation (Fig. 3) is due to re-entrainment of subducted water in the subpolar gyre and Labrador Sea, made possible by the substantial lightening of water as it moves southward into the Atlantic basin (Fig. 10). It is likely that the major source of this lightening is mixing that occurs in the vicinity of the overflows (Fig. 8).

The overflow of dense water formed in the GIN Seas into the deep Atlantic Basin, involving the turbulent entrainment of ambient water, is a process that is notoriously difficult to parameterize in numerical simulations (Legg et al. 2009). In this configuration of the NEMO ocean model, the entrainment process is not explicitly parameterized by the "bottom boundary layer" but rather is left to the implicitly diffusive nature of the tracer advection scheme (Madec 2014). Consequently, the model has no physically based "control" on the level of mixing in the region of dense overflows, with the effect that there could be excessive lightening of GIN Seas water as it flows into the Atlantic basin (Beckmann and Döscher 1997).

While the challenges of parameterizing dense water overflows are well known, the results presented here illustrate their impact on NADW ventilation and the water mass distribution of the Atlantic basin. As a result of the excessive mixing associated with the overflow parameterization, water subducted in the GIN Seas is brought back to the surface only a short distance downstream, in the Labrador Sea. This re-entrainment alters the time scale of sequestration for this water mass, whereby it is brought back in contact with the atmosphere on a time scale of years to decades rather than the centuries to millennia it would be isolated were it to remain in the deep Atlantic basin (Gebbie and Huybers 2010), with evident impact on the storage time scale of anthropogenic heat and carbon in the model. The result is that processes operating to the north of the Greenland–Scotland ridge have a substantially diminished impact on the properties of the deep ocean in this simulation.

Additionally, in the ocean, as water from the GIN Seas flows into the Atlantic basin it settles below the lighter forms of NADW formed in the Labrador and Irminger Seas (García-Ibáñez et al. 2018). The resultant deep stratification means that the overflow water masses are not penetrated by surface mixing as they are exported southward, even during times of deep convection in the Labrador Sea (Yashayaev 2007). In this simulation, an absence of deep stratification in the subpolar gyre due to excessive mixing could explain the occurrence of widespread, unrealistically deep mixed layers, particularly in the Labrador Sea, with equivalent surface forcing able to penetrate further into the weaker stratification (Kösters et al. 2005). It is clearly an open question the extent to which these impacts on NADW ventilation would be realized in a configuration adopting a different parameterization of mixing in the vicinity of overflows (e.g., Colombo et al. 2020).

5. Conclusions

A comprehensive set of Lagrangian experiments reveals the nature of North Atlantic Deep Water ventilation in an eddy-permitting numerical simulation. We found that NADW ventilation in the model is predominantly due to subduction in the Labrador Sea, helping to illustrate the distinction between regions of dense

water formation and ventilation. In addition, and contrary to expectations, a majority of the ventilation arises from subduction in the boundary current rather than the open ocean. A distinct density distribution of water masses at subduction is smoothed out in the subsurface as a result of subsurface mixing, a component of which is shown to be the result of explicit model mixing in the bottom boundary layer. Furthermore, water subducted in the Greenland–Iceland–Norwegian Seas does not form a substantial contribution of ventilated NADW due to subsurface mixing and reentrainment to the mixed layer in the Labrador Sea. Taken together, our results serve to highlight that the character of NADW ventilation, and by association uptake of anthropogenic carbon and heat, is highly sensitive to model representation of both upper ocean stratification and subsurface mixing. Such sensitivity raises important questions about the fidelity of models in representing transient climate change, particularly the sensitivity to changing surface forcing and the time scales of water mass sequestration.

Acknowledgments. At Oxford, GM was supported by Natural Environment Research Council, U.K. (Award Reference 1366286). At Princeton, GM is supported through NSF's Southern Ocean Carbon and Climate Observations and Modeling (SOCCOM) Project under the NSF Award PLR-1425989, with additional support from NOAA (Award NA18OAR4320123) and NASA (Award 80NSSC19K1115). HJ and DM were supported by the U.K. Natural Environment Research Council OSNAP Project (NE/K010948/1). LJ and RW were funded by the Joint U.K. BEIS/Defra Met Office Hadley Centre Climate Programme (GA01101). The hindcast was carried out within the European Drakkar project, and the model outputs were kindly provided by J. M. Molines and C. Talandier. We used the computational tool Ariane developed by B. Blanke and N. Grima, who also provided support and advice in its use. The authors are grateful for the comprehensive and helpful comments of three anonymous reviewers.

Data availability statement. Matlab code for reproducing the figures presented here is available on GitHub (https://github.com/gmacgilchrist/nadw). Model output used in this study can be obtained upon request to CL (camille.lique@ifremer.fr). The Lagrangian trajectory calculation software, Ariane, is available at http://stockage.univ-brest.fr/~grima/Ariane/. OSNAP data were collected and made freely available by the OSNAP (Overturning in the Subpolar North Atlantic Program) project and all the national programs that contribute to it (www.o-snap.org). The EN4 dataset is available from https://www.metoffice.gov.uk/hadobs/en4/.

REFERENCES

Abraham, J. P., and Coauthors, 2013: A review of global ocean temperature observations: Implications for ocean heat content estimates and climate change. *Rev. Geophys.*, **51**, 450–483, https://doi.org/10.1002/rog.20022.

Armi, L., 1978: Some evidence for boundary mixing in the deep ocean. *J. Geophys. Res.*, **83**, 1971–1979, https://doi.org/10.1029/JC083iC04p01971.

Bahl, A., A. Gnanadesikan, and M. A. Pradal, 2019: Variations in ocean deoxygenation across earth system models: Isolating the role of parameterized lateral mixing. *Global Biogeochem. Cycles*, **33**, 703–724, https://doi.org/10.1029/2018GB006121.

Barnier, B., and Coauthors, 2006: Impact of partial steps and momentum advection schemes in a global ocean circulation model at eddy-permitting resolution. *Ocean Dyn.*, **56**, 543–567, https://doi.org/10.1007/s10236-006-0082-1.

Barrier, N., J. Deshayes, A. M. Treguier, and C. Cassou, 2015: Heat budget in the North Atlantic subpolar gyre: Impacts of atmospheric weather regimes on the 1995 warming event. *Prog. Oceanogr.*, **130**, 75–90, https://doi.org/10.1016/j.pocean.2014.10.001.

Beadling, R. L., J. L. Russell, R. J. Stouffer, and P. J. Goodman, 2018: Evaluation of subtropical North Atlantic Ocean circulation in CMIP5 models against the observational array at 26.5°N and its changes under continued warming. *J. Climate*, **31**, 9697–9718, https://doi.org/10.1175/JCLI-D-17-0845.1.

Beckmann, A., and R. Döscher, 1997: A method for improved representation of dense water spreading over topography in geopotential-coordinate models. *J. Phys. Oceanogr.*, **27**, 581–591, https://doi.org/10.1175/1520-0485(1997)027<0581:AMFIRO>2.0.CO;2.

Blanke, B., and S. Raynaud, 1997: Kinematics of the Pacific Equatorial Undercurrent: An Eulerian and Lagrangian approach from GCM results. *J. Phys. Oceanogr.*, **27**, 1038–1053, https://doi.org/10.1175/1520-0485(1997)027<1038:KOTPEU>2.0.CO;2.

Boé, J., A. Hall, and X. Qu, 2009: Deep ocean heat uptake as a major source of spread in transient climate change simulations. *Geophys. Res. Lett.*, **36**, L22701, https://doi.org/10.1029/2009GL040845.

Bouillon, S., M. A. Morales Maqueda, V. Legat, and T. Fichefet, 2009: An elastic-viscous-plastic sea ice model formulated on Arakawa B and C grids. *Ocean Modell.*, **27**, 174–184, https://doi.org/10.1016/j.ocemod.2009.01.004.

Bower, A. S., M. S. Lozier, S. F. Gary, and C. W. Böning, 2009: Interior pathways of the North Atlantic meridional overturning circulation. *Nature*, **459**, 243–247, https://doi.org/10.1038/nature07979.

——, and Coauthors, 2019: Lagrangian views of the pathways of the Atlantic Meridional Overturning Circulation. *J. Geophys. Res. Oceans*, **124**, 5313–5335, https://doi.org/10.1029/2019JC015014.

Brodeau, L., B. Barnier, A. M. Treguier, T. Penduff, and S. Gulev, 2010: An ERA40-based atmospheric forcing for global ocean circulation models. *Ocean Modell.*, **31**, 88–104, https://doi.org/10.1016/j.ocemod.2009.10.005.

Buckley, M. W., and J. C. Marshall, 2016: Observations, inferences, and mechanisms of the Atlantic Meridional Overturning Circulation: A review. *Rev. Geophys.*, **54**, 5–63, https://doi.org/10.1002/2015RG000493.

Church, J. A., J. S. Godfrey, D. R. Jackett, and T. J. McDougall, 1991: A model of sea level rise caused by ocean thermal expansion. *J. Climate*, **4**, 438–456, https://doi.org/10.1175/1520-0442(1991)004<0438:AMOSLR>2.0.CO;2.

Colombo, P., and Coauthors, 2020: Representation of the Denmark Strait overflow in a z-coordinate eddying configuration of the NEMO (v3.6) ocean model: Resolution and parameter impacts. *Geosci. Model Dev.*, **13**, 3347–3371, https://doi.org/10.5194/gmd-13-3347-2020.

Courtois, P., X. Hu, C. Pennelly, P. Spence, and P. G. Myers, 2017: Mixed layer depth calculation in deep convection regions in ocean numerical models. *Ocean Modell.*, **120**, 60–78, https://doi.org/10.1016/j.ocemod.2017.10.007.

Cuny, J., P. B. Rhines, F. Schott, and J. R. N. Lazier, 2005: Convection above the Labrador continental slope. *J. Phys. Oceanogr.*, **35**, 489–511, https://doi.org/10.1175/JPO2700.1.

Curry, R. G., C. M. Lee, and B. Petrie, 2011: Volume, freshwater, and heat fluxes through Davis Strait, 2004–05. *J. Phys. Oceanogr.*, **41**, 429–436, https://doi.org/10.1175/2010JPO4536.1.

Cushman-Roisin, B., 1987: Subduction. *Dynamics of the Oceanic Surface Mixed Layer*, P. Muller and D. Henderson, Eds., Hawaii Institute of Geophysical Special Publications, 181–196.

de Boyer Montégut, C., G. Madec, A. S. Fischer, A. Lazar, and D. Iudicone, 2004: Mixed layer depth over the global ocean: An examination of profile data and a profile-based climatology. *J. Geophys. Res.*, **109**, C12003, https://doi.org/10.1029/2004JC002378.

de Lavergne, C., G. Madec, J. Le Sommer, A. J. Nurser, and A. C. Naveira Garabato, 2016a: The impact of a variable mixing efficiency on the abyssal overturning. *J. Phys. Oceanogr.*, **46**, 663–681, https://doi.org/10.1175/JPO-D-14-0259.1.

——, ——, ——, A. J. G. Nurser, and A. C. Naveira Garabato, 2016b: On the consumption of Antarctic Bottom Water in the abyssal ocean. *J. Phys. Oceanogr.*, **46**, 635–661, https://doi.org/10.1175/JPO-D-14-0201.1.

Dee, D. P., and Coauthors, 2011: The ERA-Interim reanalysis: Configuration and performance of the data assimilation system. *Quart. J. Roy. Meteor. Soc.*, **137**, 553–597, https://doi.org/10.1002/qj.828.

Deleersnijder, E., J. M. Campin, and E. J. Delhez, 2001: The concept of age in marine modelling I. Theory and preliminary model results. *J. Mar. Syst.*, **28**, 229–267, https://doi.org/10.1016/S0924-7963(01)00026-4.

Dickson, R., and J. Brown, 1994: The production of North Atlantic Deep Water: Sources, rates, and pathways. *J. Geophys. Res.*, **99**, 12 319–12 341, https://doi.org/10.1029/94JC00530.

Ferrari, R., and C. Wunsch, 2009: Ocean circulation kinetic energy: Reservoirs, sources, and sinks. *Annu. Rev. Fluid Mech.*, **41**, 253–282, https://doi.org/10.1146/annurev.fluid.40.111406.102139.

——, A. Mashayek, T. J. McDougall, M. Nikurashin, and J.-M. Campin, 2016: Turning ocean mixing upside down. *J. Phys. Oceanogr.*, **46**, 2239–2261, https://doi.org/10.1175/JPO-D-15-0244.1.

Fettweis, X., B. Franco, M. Tedesco, J. H. Van Angelen, J. T. Lenaerts, M. R. Van Den Broeke, and H. Gallée, 2013: Estimating the Greenland ice sheet surface mass balance contribution to future sea level rise using the regional atmospheric climate model MAR. *Cryosphere*, **7**, 469–489, https://doi.org/10.5194/tc-7-469-2013.

Frölicher, T. L., J. L. Sarmiento, D. J. Paynter, J. P. Dunne, J. P. Krasting, and M. Winton, 2015: Dominance of the Southern Ocean in anthropogenic carbon and heat uptake in CMIP5 models. *J. Climate*, **28**, 862–886, https://doi.org/10.1175/JCLI-D-14-00117.1.

García-Ibáñez, M. I., F. F. Pérez, P. Lherminier, P. Zunino, H. Mercier, and P. Tréguer, 2018: Water mass distributions and transports for the 2014 GEOVIDE cruise in the North Atlantic. *Biogeosciences*, **15**, 2075–2090, https://doi.org/10.5194/bg-15-2075-2018.

Garrett, C., P. MacCready, and P. B. Rhines, 1993: Boundary mixing and arrested Ekman layers: Rotating stratified flow near a sloping boundary. *Annu. Rev. Fluid Mech.*, **25**, 291–323, https://doi.org/10.1146/annurev.fl.25.010193.001451.

Gary, S. F., M. Susan Lozier, C. W. Böning, and A. Biastoch, 2011: Deciphering the pathways for the deep limb of the Meridional Overturning Circulation. *Deep-Sea Res. II*, **58**, 1781–1797, https://doi.org/10.1016/j.dsr2.2010.10.059.

Gebbie, G., and P. Huybers, 2010: Total matrix intercomparison: A method for determining the geometry of water-mass pathways. *J. Phys. Oceanogr.*, **40**, 1710–1728, https://doi.org/10.1175/2010JPO4272.1.

Gillard, L. C., X. Hu, P. G. Myers, and J. L. Bamber, 2016: Meltwater pathways from marine terminating glaciers of the Greenland ice sheet. *Geophys. Res. Lett.*, **43**, 10 873–10 882, https://doi.org/10.1002/2016GL070969.

Girton, J. B., and T. B. Sanford, 2003: Descent and modification of the overflow plume in the Denmark Strait. *J. Phys. Oceanogr.*, **33**, 1351–1364, https://doi.org/10.1175/1520-0485(2003)033%3c1351:DAMOTO%3e2.0.CO;2.

Good, S. A., M. J. Martin, and N. A. Rayner, 2013: EN4: Quality controlled ocean temperature and salinity profiles and monthly objective analyses with uncertainty estimates. *J. Geophys. Res. Oceans*, **118**, 6704–6716, https://doi.org/10.1002/2013JC009067.

Grégorio, S., T. Penduff, G. Sérazin, J.-M. Molines, B. Barnier, and J. Hirschi, 2015: Intrinsic variability of the Atlantic meridional overturning circulation at interannual-to-multidecadal time scales. *J. Phys. Oceanogr.*, **45**, 1929–1946, https://doi.org/10.1175/JPO-D-14-0163.1.

Griffies, S. M., R. C. Pacanowski, and R. W. Hallberg, 2000: Spurious diapycnal mixing associated with advection in a z-coordinate ocean model. *Mon. Wea. Rev.*, **128**, 538–564, https://doi.org/10.1175/1520-0493(2000)128<0538:SDMAWA>2.0.CO;2.

Groeskamp, S., A. Lenton, R. Matear, and M. Bernadette, 2016: Anthropogenic carbon in the ocean—Surface to interior connections. *Global Biogeochem. Cycles*, **30**, 1682–1698, https://doi.org/10.1002/2016GB005476.

Haine, T. W., and T. M. Hall, 2002: A generalized transport theory: Water-mass composition and age. *J. Phys. Oceanogr.*, **32**, 1932–1946, https://doi.org/10.1175/1520-0485(2002)032<1932:AGTTWM>2.0.CO;2.

Hallberg, R. W., 2013: Using a resolution function to regulate parameterizations of oceanic mesoscale eddy effects. *Ocean Modell.*, **72**, 92–103, https://doi.org/10.1016/j.ocemod.2013.08.007.

Heuzé, C., 2017: North Atlantic deep water formation and AMOC in CMIP5 models. *Ocean Sci.*, **13**, 609–622, https://doi.org/10.5194/os-13-609-2017.

Holland, M. M., J. Finnis, and M. C. Serreze, 2006: Simulated Arctic Ocean freshwater budgets in the twentieth and twenty-first centuries. *J. Climate*, **19**, 6221–6242, https://doi.org/10.1175/JCLI3967.1.

Holmes, R. M., C. de Lavergne, and T. J. McDougall, 2019: Tracer transport within abyssal mixing layers. *J. Phys. Oceanogr.*, **49**, 2669–2695, https://doi.org/10.1175/JPO-D-19-0006.1.

Holte, J., L. D. Talley, J. Gilson, and D. Roemmich, 2017: An Argo mixed layer climatology and database. *Geophys. Res. Lett.*, **44**, 5618–5626, https://doi.org/10.1002/2017GL073426.

Howatt, T., J. B. Palter, J. B. R. Matthews, B. DeYoung, R. Bachmayer, and B. Claus, 2018: Ekman and eddy exchange of freshwater and oxygen across the Labrador Shelf break. *J. Phys. Oceanogr.*, **48**, 1015–1031, https://doi.org/10.1175/JPO-D-17-0148.1.

Isachsen, P. E., C. Mauritzen, and H. Svendsen, 2007: Dense water formation in the Nordic Seas diagnosed from sea surface buoyancy fluxes. *Deep-Sea Res. I*, **54**, 22–41, https://doi.org/10.1016/j.dsr.2006.09.008.

Kamenkovich, I., Z. Garraffo, R. Pennel, and R. A. Fine, 2017: Importance of mesoscale eddies and mean circulation in ventilation of the Southern Ocean. *J. Geophys. Res. Oceans*, **122**, 2724–2741, https://doi.org/10.1002/2016JC012292.

Katavouta, A., R. G. Williams, and P. Goodwin, 2019: The effect of ocean ventilation on the transient climate response to emissions. *J. Climate*, **32**, 5085–5105, https://doi.org/10.1175/JCLI-D-18-0829.1.

Khatiwala, S., F. Primeau, and T. Hall, 2009: Reconstruction of the history of anthropogenic CO_2 concentrations in the ocean. *Nature*, **462**, 346–349, https://doi.org/10.1038/nature08526.

——, ——, and M. Holzer, 2012: Ventilation of the deep ocean constrained with tracer observations and implications for radiocarbon estimates of ideal mean age. *Earth Planet. Sci. Lett.*, **325–326**, 116–125, https://doi.org/10.1016/j.epsl.2012.01.038.

Kieke, D., M. Rhein, L. Stramma, W. M. Smethie, D. A. LeBel, and W. Zenk, 2006: Changes in the CFC inventories and formation rates of Upper Labrador Sea Water, 1997–2001. *J. Phys. Oceanogr.*, **36**, 64–86, https://doi.org/10.1175/JPO2814.1.

Klocker, A., and T. J. McDougall, 2010: Quantifying the consequences of the ill-defined nature of neutral surfaces. *J. Phys. Oceanogr.*, **40**, 1866–1880, https://doi.org/10.1175/2009JPO4212.1.

Koenigk, T., U. Mikolajewicz, H. Haak, and J. Jungclaus, 2007: Arctic freshwater export in the 20th and 21st centuries. *J. Geophys. Res.*, **112**, G04S41, https://doi.org/10.1029/2006JG000274.

Kösters, F., R. H. Käse, A. Schmittner, and P. Herrmann, 2005: The effect of Denmark Strait overflow on the Atlantic Meridional Overturning Circulation. *Geophys. Res. Lett.*, **32**, L04602, https://doi.org/10.1029/2004GL022112.

Koszalka, I. M., T. W. Haine, and M. G. Magaldi, 2013: Fates and travel times of Denmark Strait overflow water in the Irminger Basin. *J. Phys. Oceanogr.*, **43**, 2611–2628, https://doi.org/10.1175/JPO-D-13-023.1.

Kuhlbrodt, T., and J. M. Gregory, 2012: Ocean heat uptake and its consequences for the magnitude of sea level rise and climate change. *Geophys. Res. Lett.*, **39**, L18608, https://doi.org/10.1029/2012GL052952.

Lavender, K. L., R. E. Davis, and W. B. Owens, 2000: Mid-depth recirculation observed in the interior Labrador and Irminger Seas by direct velocity measurements. *Nature*, **407**, 66–69, https://doi.org/10.1038/35024048.

Lazier, J. R. N., and D. G. Wright, 1993: Annual velocity variations in the Labrador Current. *J. Phys. Oceanogr.*, **23**, 659–678, https://doi.org/10.1175/1520-0485(1993)023<0659:AVVITL>2.0.CO;2.

——, R. S. Pickart, and P. B. Rhines, 2001: Deep convection. *Ocean Circulation and Climate: Observing and Modelling the Global Ocean*, J. A. Church and J. Gould, Eds., Academic Press, 387–400.

——, R. Hendry, A. Clarke, I. M. Yashayaev, and P. B. Rhines, 2002: Convection and restratification in the Labrador Sea, 1990-2000. *Deep-Sea Res. I*, **49**, 1819–1835, https://doi.org/10.1016/S0967-0637(02)00064-X.

LeBel, D. A., and Coauthors, 2008: The formation rate of North Atlantic Deep Water and Eighteen Degree Water calculated from CFC-11 inventories observed during WOCE. *Deep-Sea Res. I*, **55**, 891–910, https://doi.org/10.1016/j.dsr.2008.03.009.

Ledwell, J. R., A. J. Watson, and C. S. Law, 1993: Evidence for slow mixing across the pycnocline from an open-ocean tracer-release experiment. *Nature*, **364**, 701–703, https://doi.org/10.1038/364701a0.

Lee, M.-M., A. C. Coward, and A. J. G. Nurser, 2002: Spurious diapycnal mixing of the deep waters in an eddy-permitting global ocean model. *J. Phys. Oceanogr.*, **32**, 1522–1535, https://doi.org/10.1175/1520-0485(2002)032<1522:SDMOTD>2.0.CO;2.

Legg, S., and Coauthors, 2009: Improving oceanic overflow representation in climate models: The gravity current entrainment climate process team. *Bull. Amer. Meteor. Soc.*, **90**, 657–670, https://doi.org/10.1175/2008BAMS2667.1.

Levitus, S., and Coauthors, 1998: *Introduction.* Vol. 1, *World Ocean Database 1998*, NOAA Atlas NESDIS 18, 346 pp.

Lique, C., and M. D. Thomas, 2018: Latitudinal shift of the Atlantic Meridional Overturning Circulation source regions under a warming climate. *Nat. Climate Change*, **8**, 1013–1020, https://doi.org/10.1038/s41558-018-0316-5.

Lozier, M. S., 2010: Deconstructing the conveyor belt. *Science*, **328**, 1507–1511, https://doi.org/10.1126/science.1189250.

——, 2012: Overturning in the North Atlantic. *Annu. Rev. Mar. Sci.*, **4**, 291–315, https://doi.org/10.1146/annurev-marine-120710-100740.

——, and Coauthors, 2017: Overturning in the subpolar North Atlantic program: A new international ocean observing system. *Bull. Amer. Meteor. Soc.*, **98**, 737–752, https://doi.org/10.1175/BAMS-D-16-0057.1.

——, and Coauthors, 2019: A sea change in our view of overturning in the subpolar North Atlantic. *Science*, **363**, 516–521, https://doi.org/10.1126/science.aau6592.

Luo, H., R. M. Castelao, A. K. Rennermalm, M. Tedesco, A. Bracco, P. L. Yager, and T. L. Mote, 2016: Oceanic transport of surface meltwater from the southern Greenland ice sheet. *Nat. Geosci.*, **9**, 528–532, https://doi.org/10.1038/ngeo2708.

MacGilchrist, G. A., D. P. Marshall, H. L. Johnson, C. Lique, and M. D. Thomas, 2017: Characterizing the chaotic nature of ocean ventilation. *J. Geophys. Res. Oceans*, **122**, 7577–7594, https://doi.org/10.1002/2017JC012875.

——, and Coauthors, 2019: Reframing the carbon cycle of the subpolar Southern Ocean. *Sci. Adv.*, **5**, eaav6410, https://doi.org/10.1126/sciadv.aav6410.

MacKinnon, J. A., and Coauthors, 2017: Climate process team on internal wave-driven ocean mixing. *Bull. Amer. Meteor. Soc.*, **98**, 2429–2454, https://doi.org/10.1175/BAMS-D-16-0030.1.

MacLachlan, C., and Coauthors, 2015: Global Seasonal forecast system version 5 (GloSea5): A high-resolution seasonal forecast system. *Quart. J. Roy. Meteor. Soc.*, **141**, 1072–1084, https://doi.org/10.1002/qj.2396.

Madec, G., 2014: NEMO ocean engine. Note du Pole de Modelisation de l'Institut Pierre-Simon Laplace Tech. Rep. 27.

Marsh, R., 2000: Recent variability of the North Atlantic thermohaline circulation inferred from surface heat and freshwater fluxes. *J. Climate*, **13**, 3239–3260, https://doi.org/10.1175/1520-0442(2000)013<3239:RVOTNA>2.0.CO;2.

Marshall, D. P., and J. C. Marshall, 1995: On the thermodynamics of subduction. *J. Phys. Oceanogr.*, **25**, 138–151, https://doi.org/10.1175/1520-0485(1995)025<0138:OTTOS>2.0.CO;2.

Marshall, J. C., A. J. G. Nurser, and R. G. Williams, 1993: Inferring the subduction rate and period over the North Atlantic. *J. Phys. Oceanogr.*, **23**, 1315–1329, https://doi.org/10.1175/1520-0485(1993)023<1315:ITSRAP>2.0.CO;2.

Mashayek, A., R. Ferrari, S. Merrifield, J. R. Ledwell, L. S. Laurent, and A. N. Garabato, 2017: Topographic enhancement of vertical turbulent mixing in the Southern Ocean. *Nat. Commun.*, **8**, 14197, https://doi.org/10.1038/NCOMMS14197.

Mauritzen, C., J. Price, T. Sanford, and D. Torres, 2005: Circulation and mixing in the Faroese Channels. *Deep-Sea Res. I*, **52**, 883–913, https://doi.org/10.1016/j.dsr.2004.11.018.

McDougall, T. J., 1987: Thermobaricity, cabbeling, and water-mass conversion. *J. Geophys. Res.*, **92**, 5448–5464, https://doi.org/10.1029/JC092iC05p05448.

——, and D. R. Jackett, 2005: The material derivative of neutral density. *J. Mar. Res.*, **63**, 159–185, https://doi.org/10.1357/0022240053693734.

Megann, A., 2018: Estimating the numerical diapycnal mixing in an eddy-permitting ocean model. *Ocean Modell.*, **121**, 19–33, https://doi.org/10.1016/j.ocemod.2017.11.001.

Naveira Garabato, A. C., G. A. MacGilchrist, P. J. Brown, D. G. Evans, A. J. S. Meijers, and J. D. Zika, 2017: High-latitude ocean ventilation and its role in Earth's climate transitions. *Philos. Trans. Roy. Soc. London*, **375A**, 20160324, https://doi.org/10.1098/rsta.2016.0324.

Palter, J. B., M. S. Lozier, and K. L. Lavender, 2008: How does Labrador Sea water enter the deep western boundary current? *J. Phys. Oceanogr.*, **38**, 968–983, https://doi.org/10.1175/2007JPO3807.1.

Pennelly, C., X. Hu, and P. G. Myers, 2019: Cross-isobath freshwater exchange within the North Atlantic subpolar gyre. *J. Geophys. Res. Oceans*, **124**, 6831–6853, https://doi.org/10.1029/2019JC015144.

Pickart, R. S., 1992: Water mass components of the North Atlantic deep western boundary current. *Deep-Sea Res. I*, **39**, 1553–1572, https://doi.org/10.1016/0198-0149(92)90047-W.

——, and M. A. Spall, 2007: Impact of Labrador Sea convection on the North Atlantic meridional. *J. Phys. Oceanogr.*, **37**, 2207–2227, https://doi.org/10.1175/JPO3178.1.

——, ——, and J. R. N. Lazier, 1997: Mid-depth ventilation in the western boundary current system of the sub-polar gyre. *Deep-Sea Res. I*, **44**, 1025–1054, https://doi.org/10.1016/S0967-0637(96)00122-7.

——, D. J. Torres, and A. Clarke, 2002: Hydrography of the Labrador Sea during active convection. *J. Phys. Oceanogr.*, **32**, 428–457, https://doi.org/10.1175/1520-0485(2002)032<0428:HOTLSD>2.0.CO;2.

Primeau, F., 2005: Characterizing transport between the surface mixed layer and the ocean interior with a forward and adjoint global ocean transport model. *J. Phys. Oceanogr.*, **35**, 545–564, https://doi.org/10.1175/JPO2699.1.

Qiu, B., and R. X. Huang, 1995: Ventilation of the North Atlantic and North Pacific: Subduction versus obduction. *J. Phys. Oceanogr.*, **25**, 2374–2390, https://doi.org/10.1175/1520-0485(1995)025<2374:VOTNAA>2.0.CO;2.

Rattan, S., P. G. Myers, A. M. Treguier, S. Theetten, A. Biastoch, and C. Böning, 2010: Towards an understanding of Labrador Sea salinity drift in eddy-permitting simulations. *Ocean Modell.*, **35**, 77–88, https://doi.org/10.1016/j.ocemod.2010.06.007.

Rhein, M., D. Kieke, and R. Steinfeldt, 2007: Ventilation of the Upper Labrador Sea Water, 2003–2005. *Geophys. Res. Lett.*, **34**, L06603, https://doi.org/10.1029/2006GL028540.

——, ——, and ——, 2015: Advection of North Atlantic Deep Water from the Labrador Sea to the Southern Hemisphere. *J. Geophys. Res. Oceans*, **120**, 2471–2487, https://doi.org/10.1002/2014JC010605.

Rühs, S., J. V. Durgadoo, E. Behrens, and A. Biastoch, 2013: Advective timescales and pathways of Agulhas leakage. *Geophys. Res. Lett.*, **40**, 3997–4000, https://doi.org/10.1002/grl.50782.

Sabine, C. L., and Coauthors, 2004: The oceanic sink for anthropogenic CO_2. *Science*, **305**, 367–371, https://doi.org/10.1126/science.1097403.

Saenko, O. A., F. Dupont, D. Yang, P. G. Myers, I. M. Yashayaev, and G. C. Smith, 2014: Role of resolved and parameterized eddies in the Labrador Sea balance of heat and buoyancy. *J. Phys. Oceanogr.*, **44**, 3008–3032, https://doi.org/10.1175/JPO-D-14-0041.1.

Shah, S. H. A. M., A. W. Heemink, and E. Deleersnijder, 2011: Assessing Lagrangian schemes for simulating diffusion on non-flat isopycnal surfaces. *Ocean Modell.*, **39**, 351–361, https://doi.org/10.1016/j.ocemod.2011.05.008.

——, F. Primeau, E. Deleersnijder, and A. W. Heemink, 2017: Tracing the ventilation pathways of the deep North Pacific Ocean using Lagrangian particles and Eulerian tracers. *J. Phys. Oceanogr.*, **47**, 1261–1280, https://doi.org/10.1175/JPO-D-16-0098.1.

Spall, M. A., 2004: Boundary currents and watermass transformation in marginal seas. *J. Phys. Oceanogr.*, **34**, 1197–1213, https://doi.org/10.1175/1520-0485(2004)034<1197:BCAWTI>2.0.CO;2.

——, and R. S. Pickart, 2001: Where does dense water sink? A subpolar gyre example. *J. Phys. Oceanogr.*, **31**, 810–826, https://doi.org/10.1175/1520-0485(2001)031<0810:WDDWSA>2.0.CO;2.

Stommel, H. M., 1979: Determination of water mass properties of water pumped down from the Ekman layer to the geostrophic flow below. *Proc. Natl. Acad. Sci. USA*, **76**, 3051–3055, https://doi.org/10.1073/pnas.76.7.3051.

Straneo, F., 2006: Heat and freshwater transport through the central Labrador Sea. *J. Phys. Oceanogr.*, **36**, 606–628, https://doi.org/10.1175/JPO2875.1.

——, and F. J. Saucier, 2008: The Arctic–Subarctic exchange through Hudson Strait. *Arctic–Subarctic Ocean Fluxes: Defining the Role of Northern Seas in Climate*, R. R. Dickson, J. Meincke, and P. Rhines, Eds., Springer, 249–261.

Swingedouw, D., C. B. Rodehacke, S. M. Olsen, M. Menary, Y. Gao, U. Mikolajewicz, and J. Mignot, 2015: On the reduced sensitivity of the Atlantic overturning to Greenland ice sheet melting in projections: A multi-model assessment. *Climate Dyn.*, **44**, 3261–3279, https://doi.org/10.1007/s00382-014-2270-x.

Talley, L. D., 2013: Closure of the global overturning circulation through the Indian, Pacific, and Southern Oceans: Schematics and transports. *Oceanography*, **26**, 80–97, https://doi.org/10.5670/oceanog.2013.07.

——, and M. S. McCartney, 1982: Distribution and circulation of Labrador Sea Water. *J. Phys. Oceanogr.*, **12**, 1189–1205, https://doi.org/10.1175/1520-0485(1982)012<1189:DACOLS>2.0.CO;2.

Thomas, M. D., A. Treguier, B. Blanke, J. Deshayes, and A. Voldoire, 2015: A Lagrangian method to isolate the impacts of mixed layer subduction on the meridional overturning circulation in a numerical model. *J. Climate*, **28**, 7503–7517, https://doi.org/10.1175/JCLI-D-14-00631.1.

Tuerena, R. E., R. G. Williams, C. Mahaffey, C. Vic, J. A. Green, A. Naveira-Garabato, A. Forryan, and J. Sharples, 2019: Internal tides drive nutrient fluxes into the deep chlorophyll maximum over mid-ocean ridges. *Global Biogeochem. Cycles*, **33**, 995–1009, https://doi.org/10.1029/2019GB006214.

Våge, K., and Coauthors, 2011: The Irminger Gyre: Circulation, convection, and interannual variability. *Deep-Sea Res. I*, **58**, 590–614, https://doi.org/10.1016/j.dsr.2011.03.001.

van Sebille, E., M. O. Baringer, W. E. Johns, C. S. Meinen, L. M. Beal, M. F. De Jong, and H. M. Van Aken, 2011: Propagation pathways of classical Labrador Sea water from its source region to 26°N. *J. Geophys. Res.*, **116**, C12027, https://doi.org/10.1029/2011JC007171.

——, and Coauthors, 2018: Lagrangian ocean analysis: Fundamentals and practices. *Ocean Modell.*, **121**, 49–75, https://doi.org/10.1016/j.ocemod.2017.11.008.

Waterhouse, A. F., and Coauthors, 2014: Global patterns of diapycnal mixing from measurements of the turbulent dissipation rate. *J. Phys. Oceanogr.*, **44**, 1854–1872, https://doi.org/10.1175/JPO-D-13-0104.1.

Williams, R. G., M. A. Spall, and J. C. Marshall, 1995: Does Stommel's mixed layer "demon" work? *J. Phys. Oceanogr.*, **25**, 3089–3102, https://doi.org/10.1175/1520-0485(1995)025<3089:DSMLW>2.0.CO;2.

Yashayaev, I. M., 2007: Hydrographic changes in the Labrador Sea, 1960–2005. *Prog. Oceanogr.*, **73**, 242–276, https://doi.org/10.1016/j.pocean.2007.04.015.

——, and J. W. Loder, 2016: Recurrent replenishment of Labrador Sea Water and associated decadal-scale variability. *J. Geophys. Res. Oceans*, **121**, 8095–8114, https://doi.org/10.1002/2016JC012046.

Zanna, L., S. Khatiwala, J. M. Gregory, J. Ison, and P. Heimbach, 2019: Global reconstruction of historical ocean heat storage and transport. *Proc. Natl. Acad. Sci. USA*, **116**, 1126–1131, https://doi.org/10.1073/pnas.1808838115.

Zou, S., M. S. Lozier, F. Li, R. Abernathey, and L. Jackson, 2020: Density-compensated overturning in the Labrador Sea. *Nat. Geosci.*, **13**, 121–126, https://doi.org/10.1038/s41561-019-0517-1.